

Impact of a scale-aware convective parameterization scheme on the simulation of convective cells related heavy rainfall in South Korea

Haerin Park¹, Gayoung Kim¹, Dong-Hyun Cha¹, Eun-Chul Chang², Joowan Kim², Sang-Hun Park³, and Dong-Kyou Lee⁴

¹Ulsan National Institute of Science and Technology

²Kongju National University

³Yonsei University

⁴Seoul National University

November 22, 2022

Abstract

This study investigates the impact of the scale-aware convective parameterization scheme (CPS) on convective cells related to simulation of heavy precipitation across the gray-zone using the Weather Research and Forecasting (WRF) model. We select the Kain-Fritsch (KF) and Multi-scale Kain-Fritsch (MSKF) schemes as non-scale-aware and scale-aware CPSs, respectively. The MSKF scheme uses a scale-aware parameter that modulates the convective available potential energy (CAPE) timescale and entrainment process in the KF scheme as a function of the horizontal grid spacing. This study shows that simulation of convection only with grid-scale process microphysics parameterization scheme (MPS) (i.e., explicitly resolved) causes an unreasonably overestimated and erroneous location of precipitation in the gray-zone because convection and atmospheric instability could not properly be triggered and reduced. Contrarily, the CPS without scale-awareness in the gray-zone exaggerates the convection and distorts synoptic fields leading to the erroneous simulation of heavy precipitation at high resolution. Contrastingly, the MSKF scheme with scale-awareness improves simulated convective cells related to heavy rainfall by removing atmospheric instability in the gray-zone, smoothly reducing the role of CPS and increasing the role of MPS as grid spacing is decreased. Additionally, the sensitivity experiments show that the shorter CAPE timescale and decreased entrainment process resulted in fast development and exaggeration of convective activities, respectively. These parameters modulated by the scale-aware MSKF scheme can play a crucial role in the balanced effect between the CPS and MPS in the gray-zone by controlling the entrainment rate and CAPE timescale.

Hosted file

james_suppoting_park et al.docx available at <https://authorea.com/users/535912/articles/598895-impact-of-a-scale-aware-convective-parameterization-scheme-on-the-simulation-of-convective-cells-related-heavy-rainfall-in-south-korea>

1 **Impact of a scale-aware convective parameterization scheme on the simulation of**
2 **convective cells related heavy rainfall in South Korea**
3

4 **Haerin Park¹, Gayoung Kim¹, Dong-Hyun Cha¹, Eun-Chul Chang², Joowan Kim², Sang-**
5 **Hun Park³, Dong-Kyou Lee⁴**

6 ¹ Department of Urban & Environmental Engineering, Ulsan National Institute of Science and
7 Technology, Ulsan, South Korea

8 ² Department of Atmospheric Sciences, Kongju National University, Kongju, South Korea

9 ³ Department of Atmospheric Sciences, Yonsei University, Seoul, South Korea

10 ⁴ School of Earth and Environmental Sciences, Seoul National University, Seoul, South Korea

11
12 Corresponding author: Dong-Hyun Cha (dhcha@unist.ac.kr)

13 †School of Urban and Environmental Engineering

14 Ulsan National Institute of Science & Technology (UNIST)

15 50 UNIST-gil, Ulsu-gun, Ulsan 689-798, South Korea

16 Office) +82-52-217-2828, Fax) +82-52-217-2809

17
18
19 **Key Points:**

- 20 • We investigated the impact of the scale-aware convective parameterization scheme across
21 the gray-zone using the WRF model.
22
23 • The scale-aware CPS improved simulated convective cells related to rainfall by properly
24 removing atmospheric instability in the gray-zone.
25
26 • CAPE timescale and entrainment rate modulated in the scale-aware MSKF are the key
27 parameters for the improved rainfall simulation in the gray-zone.

28 Abstract

29 This study investigates the impact of the scale-aware convective parameterization scheme (CPS)
30 on convective cells related to simulation of heavy precipitation across the gray-zone using the
31 Weather Research and Forecasting (WRF) model. We select the Kain-Fritsch (KF) and Multi-
32 scale Kain-Fritsch (MSKF) schemes as non-scale-aware and scale-aware CPSs, respectively. The
33 MSKF scheme uses a scale-aware parameter that modulates the convective available potential
34 energy (CAPE) timescale and entrainment process in the KF scheme as a function of the
35 horizontal grid spacing. This study shows that simulation of convection only with grid-scale
36 process microphysics parameterization scheme (MPS) (i.e., explicitly resolved) causes an
37 unreasonably overestimated and erroneous location of precipitation in the gray-zone because
38 convection and atmospheric instability could not properly be triggered and reduced. Contrarily,
39 the CPS without scale-awareness in the gray-zone exaggerates the convection and distorts
40 synoptic fields, leading to the erroneous simulation of heavy precipitation at high resolution.
41 Contrastingly, the MSKF scheme with scale-awareness improves simulated convective cells
42 related to heavy rainfall by removing atmospheric instability in the gray-zone, smoothly reducing
43 the role of CPS and increasing the role of MPS as grid spacing is decreased. Additionally, the
44 sensitivity experiments show that the shorter CAPE timescale and decreased entrainment process
45 resulted in fast development and exaggeration of convective activities, respectively. These
46 parameters modulated by the scale-aware MSKF scheme can play a crucial role in the balanced
47 effect between the CPS and MPS in the gray-zone by controlling the entrainment rate and CAPE
48 timescale.

49 Plain Language Summary

50 With the increasing computer resources, Numerical weather prediction (NWP) models are
51 operating in the "gray zone" at horizontal grid spacing in the range of 1-10 km, where both
52 cumulus parameterization and explicit resolve are problematic. This study investigates the
53 impact of the scale-aware convective parameterization scheme (CPS) on convective cells in the
54 simulation of heavy precipitation across the gray-zone using the Weather Research and
55 Forecasting (WRF) model. The scale-aware CPS uses a scale-aware parameter that modulates
56 the convective process as a function of the horizontal grid spacing. We found that simulating
57 convection processes in the gray-zone without CPS is still limited because atmospheric
58 instability inadequately triggers or reduces it. Moreover, the CPS without scale-awareness
59 caused the erroneous precipitation simulation due to the exaggeration of convection and
60 distortion of the synoptic fields. Contrastingly, the scale-aware CPS improved the simulated
61 convection cells associated with heavy rainfall in the gray-zone by reducing the role of CPS and
62 increasing the role of explicitly resolved precipitation as grid spacing is decreased. Results
63 indicated that including scale-aware parameter in scale-awareness CPS plays a crucial role in
64 controlling the CPS and MPS in the gray-zone by controlling the convective processes.

65 **1 Introduction**

66 The precipitation characteristics in Korea have altered due to a changing climate. *Ha et*
67 *al.* (2005) and *Kwon et al.* (2007) showed that the East Asian summer monsoon changed since
68 the early mid-1990s. Several studies have shown that annual rainfall in Korea has tended to
69 increase. Notably, the frequency and intensity of precipitation increased considerably since the
70 1990s (*Kim et al.*, 2008; *Choi et al.*, 2013; *Mun et al.*, 2019). *Choi et al.* (2008) showed that
71 precipitation, especially in July and August, increased significantly. *Lee et al.* (2011a) indicated
72 that the annual precipitation amount from 2001 to 2010 considerably increased in July compared

73 to the past 30 years from 1970 to 2000. *Ho et al.* (2003) showed that the precipitation intensity in
74 early August was significantly enhanced due to the spatial difference in mid-level geopotential
75 height over the whole of Asia as a result of global warming. More than half of the annual
76 precipitation in Korea is concentrated in the summer (*Ho&Kang*, 1988; *Park et al.*, 2008), and
77 heavy rainfall during the summer monsoon is one of the robust characteristics of precipitation in
78 Korea, which causes considerable socioeconomic damage (*Kang et al.*, 1992). Various
79 precipitation systems generate heavy rainfall over the Korean Peninsula (e.g., band-type and
80 cluster) (*Sun&Lee*, 2002; *Shin&Lee*, 2005; *Cho&Lee*, 2006). Mesoscale convective systems
81 (MCSs) are the major types of heavy rainfall systems, which act over the Korean Peninsula
82 during the summer monsoon. Approximately 47% of heavy rainfall events between 2000 and
83 2006 were associated with MCSs (*Lee&Kim*, 2007). According to the Korean Ministry of the
84 Interior and Safety, the average annual number of death and the total property damages due to
85 heavy precipitation from 2009 to 2018 are 11.5 people and \$125 million, respectively (*MOIS*,
86 2019). More reliable and accurate predictions and a better understanding of the formation and
87 development mechanisms using observation data and numerical models are necessary to reduce
88 damage caused by heavy precipitation in Korea.

89 Many studies utilized a coarser horizontal grid spacing of the numerical models than the
90 actual horizontal scale of cumulus convection due to the limitation of computing resources. At
91 coarser resolutions with grid spacing larger than 10 km, the convective parameterization scheme
92 (CPS) is turned on to represent the effect of subgrid-scale convection on large-scale fields by
93 calculating the potential subgrid-scale cloud and physics of precipitation processes in association
94 with grid-scale independent and dependent variables. With the CPS, subgrid-scale convection is
95 possible even if the air parcel at the grid point is not saturated. Therefore, the CPS reduces delay

96 in precipitation or local instability, and it can represent the interaction between clouds and the
97 surrounding environment (*Bechtold et al.*, 2014; *Freitas et al.*, 2018; *Han et al.*, 2011). Many
98 studies (*Wang&Seaman*, 1997; *Yang et al.*, 2000) have shown that numerical simulation can be
99 sensitive to the chosen parameterization schemes compared to those of the other factors (e.g.,
100 domain setup and studied cases). *Jankov et al.* (2007) and *Lowrey and Yang* (2008) indicated that
101 the different parameterization schemes (e.g., CPS and microphysics parameterization scheme
102 (MPS)) resulted in different simulation results, and especially the CPS showed a significant
103 impact on precipitation simulation. Parameterized convection at coarse horizontal grid spacing
104 has limitations and causes inaccurate precipitation simulations (e.g., *Emanuel&Raymond*, 1993;
105 *Olson et al.*, 1995; *Wang&Seaman*, 1997). Therefore, efforts to improve the CPS are required to
106 reduce the prediction error of the convection process in the subgrid-scale (*Wang et al.*, 2006;
107 *Dudhia*, 2005).

108 According to tremendous numerical computing and atmospheric modeling technology
109 that can support high-resolution modeling, the grid sizes of numerical weather models are now
110 close to 2–10 km (*Davies et al.*, 2005; *Saito et al.*, 2006; *Charles et al.*, 2009). Although a higher
111 resolution allows for more accurate representations of surface fields and topography, it is
112 generally difficult to define the range of convection process between the subgrid-scale to be
113 parameterized using CPS and the grid-scale to be explicitly resolved (*Hong&Dudhia*, 2012;
114 *Molinari&Dudek*, 1992; *Jeworrek et al.*, 2019), which is called “gray-zone (1–10 km)”
115 (*Gerard&oceanography*, 2007). The development of CPS for the gray-zone in the numerical
116 model remains a problem (*Hong&Dudhia*, 2012).

117 Generally, the CPS is not required as explicitly resolved convections are considered
118 sufficient in grid intervals under the gray-zone. *Wang et al.* (2015) shows that the regional

119 models with 9-km grid spacing can capture the salient characteristics of precipitation over the
120 tropics without CPS. In *Molinari and Dudek (1992)* and *Weisman et al. (1997)*, the horizontal
121 grid spacing is 4 km or less, and it can explicitly consider convection-permitting without relying
122 on CPS at this resolution. *Yu et al. (2010)* indicate that a grid size of 3 km is sufficient to resolve
123 the convection band and CPS for this grid size is not necessary.

124 Contrarily, studies have shown that high-resolution numerical models only with MPS
125 (i.e., no CPS) still have limitations in simulating convection processes (*Arakawa et al., 2016*;
126 *Gustafson et al., 2013*). *Deng et al. (2006)* showed that the simulated precipitation skill of a 4-
127 km grid improved when CPS was used. Furthermore, *Lee et al. (2011b)* showed that the
128 numerical model improves heavy rainfall forecast by activating both the CPS and MPS at fine
129 grid size (e.g., 3 km). There are still ambiguous results for the CPS activation at grid spacings
130 smaller than 3 and 4 km. Consequentially, there remains an effort to adjust or improve the CPS
131 validity in the gray-zone (*Arakawa et al., 2011*; *Hong&Dudhia, 2012*; *Prein et al., 2015*;
132 *Bengtsson&Körnich, 2016*; *Zheng et al., 2016*). Such new schemes are designed to be scale-
133 aware, such that they can represent smooth transition grid intervals. *Sims et al. (2017)* showed
134 that an applied scale-aware parameter, which is a function of horizontal resolution, determined
135 the simulation performance of mesoscale convection phenomena, and the Kain-Fritsch scheme
136 (KF) modified by the scale-aware parameter could improve the convection timing of the
137 mesoscale convection phenomenon in the Carolinas region. *Kwon and Hong (2017)* applied the
138 scale-aware parameters in the Simplified Arakawa-Schubert scheme at 3 km, which improved
139 simulated precipitation over the Korean Peninsula by the summer monsoon. A study by *Jeworrek*
140 *et al. (2019)* consisted of five domains with different horizontal model resolutions (27, 9, 3, 1,
141 and 0.3 km) to investigate the predictability of the CPSs with scale-aware parameters in the gray-

142 zone. Their study testing the effect of scale-aware CPS showed significant improvement in the
143 location, pattern, and intensity of precipitation at high resolution. The role of CPS is gradually
144 reduced to reproduce the smooth reduction from subgrid-scale to grid-scale precipitation with
145 increasing resolution.

146 Summarily, the physics of the sub-grid precipitation process plays an essential role in the
147 simulation of precipitation over the Korean Peninsula, and studies showed that the importance of
148 smooth CPS activation using scale-aware parameters increased with higher resolution (*Alapaty et*
149 *al.*, 2012; *Sims et al.*, 2017; *Kwon&Hong*, 2017; *Jeworrek et al.*, 2019). Thus far, various
150 numerical studies have been conducted to understand the effect of high-resolution models in
151 simulating heavy rainfall events over the Korean Peninsula (*Hong&Lee*, 2009; *Kwon&Hong*,
152 2017). However, studies on the role of scale-aware parameterization schemes in the gray-zone
153 are still limited for heavy rainfall cases in the Korean Peninsula. Therefore, this study
154 investigated the effect of scale-aware parameters on a gray-zone domain using non-scale-aware
155 and scale-aware CPS for a heavy rainfall case in Korea. In this study, the KF (*Kain*, 2004) and
156 the Multi-scale Kain-Fritsch (MSKF) schemes (*Zheng et al.*, 2016) are selected for CPSs. The
157 MSKF scheme is a scale-aware version of the KF scheme, in which the CAPE timescale and
158 entrainment rate are adjusted according to the horizontal grid spacing. A flash flooding event in
159 the central region of the Korean Peninsula from 15 to 17 July 2017, is selected as the heavy
160 rainfall case. The case is spatially and temporally localized and is suitable for analyzing
161 precipitation sensitivity to the applied non-scale and scale-aware CPS in the gray-zone.

162 Simulations of numerical models are influenced by various CPS factors, such as the
163 CAPE timescale and entrainment rate. In the model, the CAPE timescale plays a role in the
164 dissipation of the deep moist convection instability during that period and determines the cloud

165 lifetime (*Mishra&Srinivasan*, 2010). Additionally, the entrainment rate changes the convective
166 process by determining the saturation and mixing with the surrounding dry air (*Lin&Arakawa*,
167 1997; *Kuang&Bretherton*, 2006; *Khairoutdinov&Randall*, 2006). Therefore, we conducted
168 sensitivity experiments to examine the impacts of the scale-aware parameter on the CAPE
169 timescale and entrainment rate in the MSKF scheme.

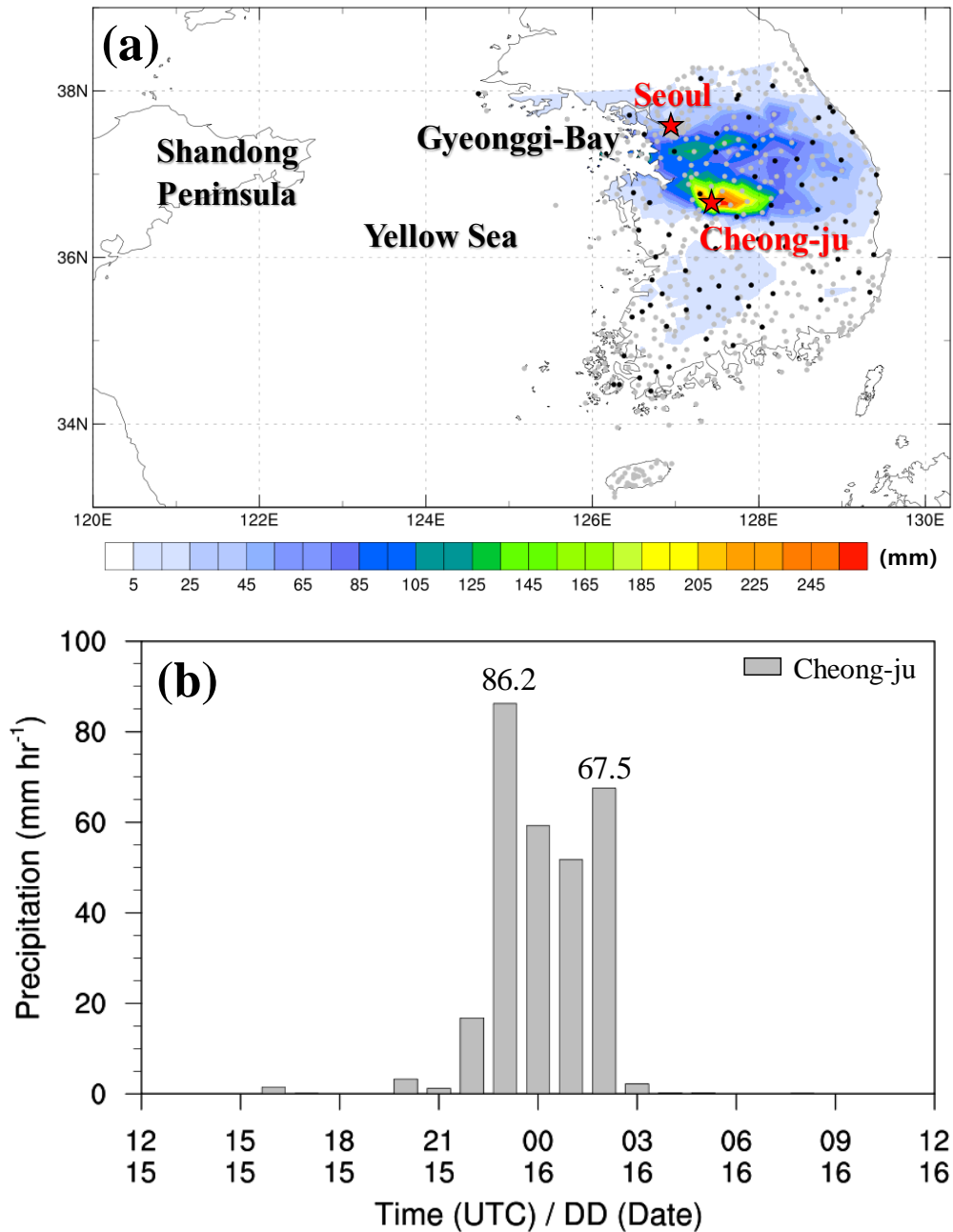
170 The rest of the paper is organized as follows. Section 2 describes the studied heavy
171 rainfall case and numerical experimental design. Section 3 shows the results from the numerical
172 experiments with different CPSs and sensitivities to the scale-aware parameter. Finally, the
173 summary and conclusions are provided in Section 4.

174 **2 Case and Experimental Design**

175 2.1 Characteristics of Cheong-ju rainfall case

176 A significant amount of extreme precipitation was recorded in Cheong-ju city on 16 July
177 2017 (Figure 1a), with a maximum daily rainfall of 290.2 mm. In Choeng-ju (marked as a red
178 star in Figure 1a), the rainfall started at 2000 UTC, 15 July (0500 LST, 16 July), and the first and
179 second peaks occurred at 2300 UTC, 15 July and 0200 UTC, 16 July, respectively (Figure 1b).
180 Hourly rainfall rates peaked at 2300 UTC with 86.2 mm hr⁻¹ and 0200 UTC with 67.5 mm hr⁻¹.
181 Subsequently, the rainfall almost stopped at 0300 UTC on 16 July 2017.

182



183

184 **Figure 1.** (a) Map of the study area showing the 24-hour accumulated rainfall amounts (mm)
 185 observed by automated surface observation systems (ASOS, black dots) and automatic weather
 186 stations (AWS, gray dots) in the central Korean Peninsula from 1200 UTC (2100 LST), 15 to
 187 1200 UTC (2100 LST), 16 July 2017 (The star mark denotes the location of Seoul and Cheong-
 188 ju), and (b) Bar plot of the time series of hourly rainfall from Cheong-ju, from
 189 1200 UTC (2100 LST), 15 to 1200 UTC (2100 LST), 16 July 2017.

190

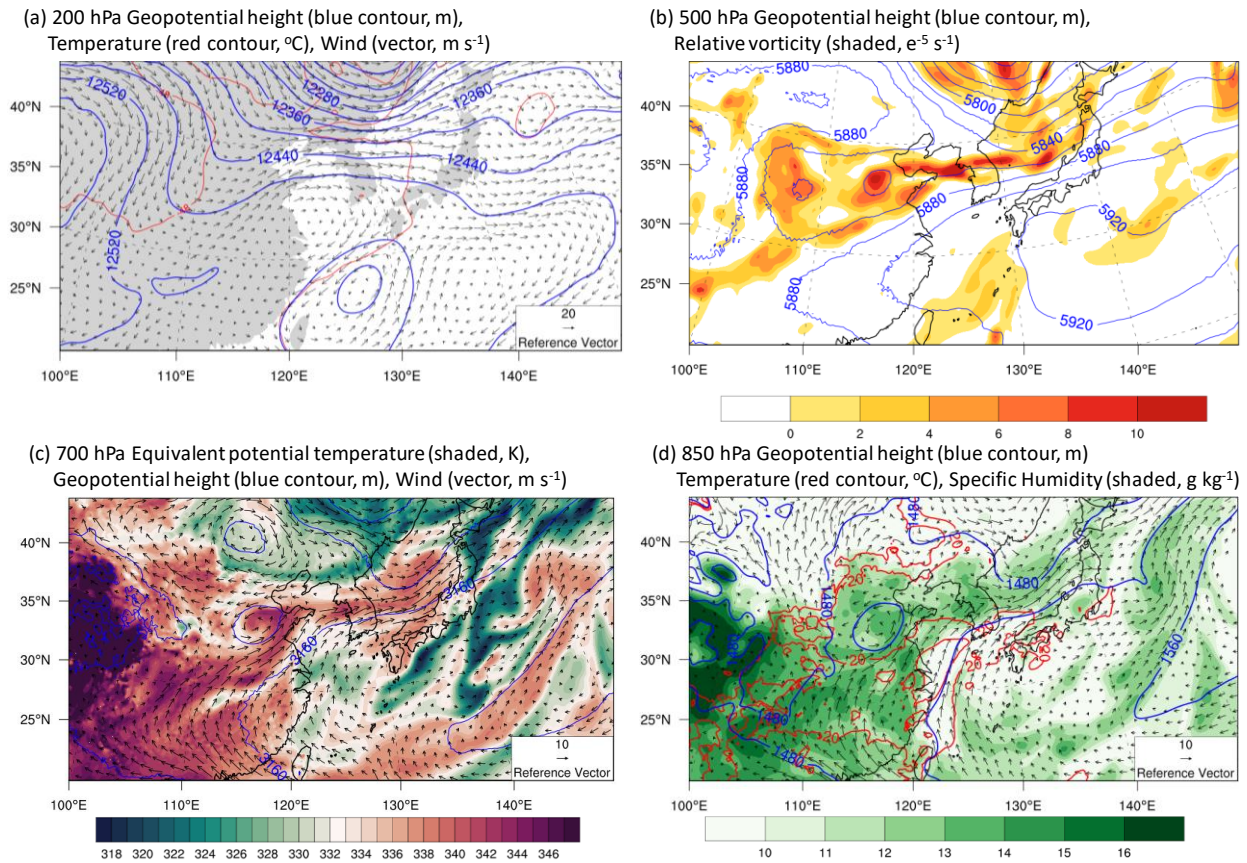
191

192 Figure 2 shows the synoptic fields of four pressure levels analyzed by the FNL 0.25°
193 reanalysis data at 1800 UTC, 15 July 2017, which was 6 h before the maximum precipitation
194 intensity in Cheong-ju. At 200 hPa (Figure 2a), an upper-pressure trough developed west of the
195 Shandong Peninsula and a shallow upper-pressure ridge in the south of the Shandong Peninsula
196 extending to South Korea. Figure 2b and d show that the western North Pacific subtropical high
197 (WNPSH) is expanded to the Korean Peninsula, forming a confluent flow region, and warm and
198 humid water vapor is transported into the central region in the Korean Peninsula. Notably,
199 positive relative vorticity is dominant over the central region of the Korean Peninsula, where the
200 southwesterly enhances continuous moisture transportation (Figure 2b). Additionally, the
201 divergence areas are consistent with the water vapor convergent flow areas at the lower level
202 (i.e., the Shandong Peninsula and the Korean Peninsula), indicating that both dynamic and
203 thermodynamic environments induced rising motion at the mid-level (see supplementary Figure
204 S1). Due to the unstable conditions, the quasi-stationary front (Changma front) is initiated from
205 the west of the Shandong Peninsula (along the isotherm of 333 K in Figure 2c), where a robust
206 upper-level trough expands to the Korean Peninsula. Environmental conditions such as upper-
207 level divergence, abundant water vapor supply, and significant atmospheric instability are
208 favorable for developing a convection system. *Chung et al. (2019)* found that warming in the
209 northern part of the Changma front resulted in less meridional temperature contrast and an
210 unstable atmosphere repeating a small disturbance that has moved along the boundary in the
211 WNPSH, which resulted in discontinuous cloud bands and intermittent rainfall. A discontinuous
212 broken Changma front with strong convective cells is represented through the 3-hourly enhanced
213 IR satellite images from 1600 UTC, 15 July to 0100 UTC, 16 July (Figure 3). In the enhanced IR
214 images, there are two convective cells: a convective cell (hereafter referred to as CC1) that has

215 begun to develop off the coast of Gyeonggi-bay and a deep-developed convective cell (hereafter
 216 called CC2) in the south of Shandong Peninsula. Eventually, the CC1 generated on Gyeonggi-
 217 bay gradually developed and advanced to the southeast (Figure 3a and b). All precipitation of
 218 this investigated event was associated with CC1. Another convective cell (i.e., CC2) developed
 219 in the south of the Shandong Peninsula, which moved into the Yellow Sea over time. These
 220 cloud systems result from the rising motion and substantial low-level convergent area from the
 221 activated quasi-stationary front accompanied by heavy rainfall.

222

223

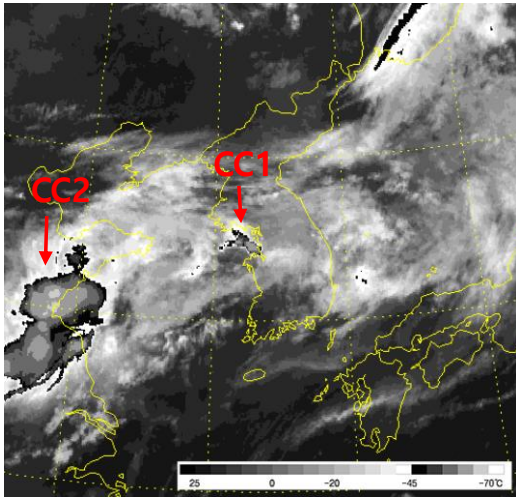


224

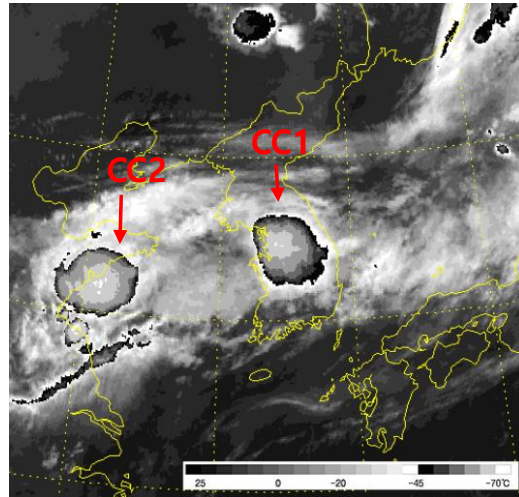
225 **Figure 2.** Spatial contour maps showing the synoptic fields from FNL 0.25° reanalysis data at
 226 1800 UTC, 15 July 2017.

227

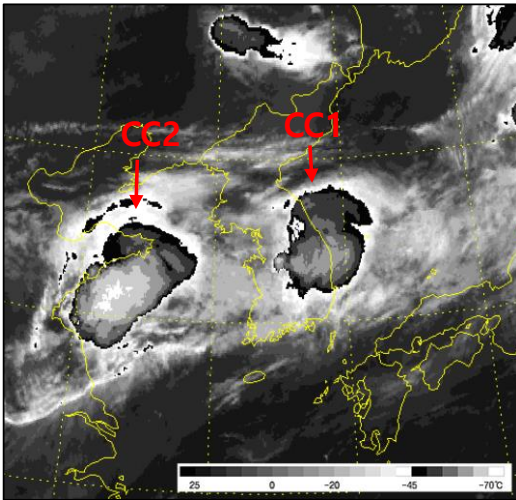
(a) 1600 UTC July 15



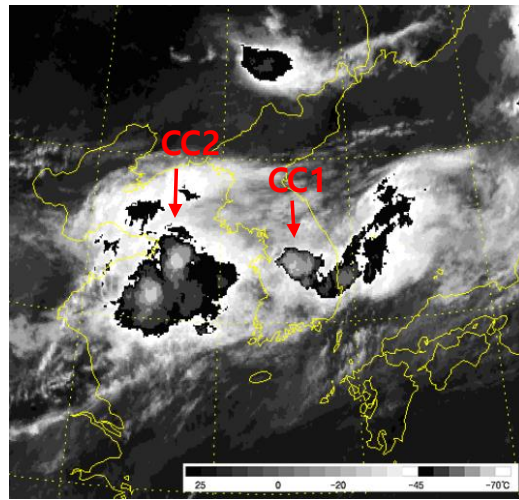
(b) 1900 UTC July 15



(c) 2200 UTC July 15



(d) 0100 UTC July 16



228
229

230 **Figure 3.** Three-hourly Enhanced IR satellite images showing cloud system development between
231 1600 UTC, 15 July and 0100 UTC, 16 July 2017.

232
233

234 2.2 Model configuration and experiment design

235

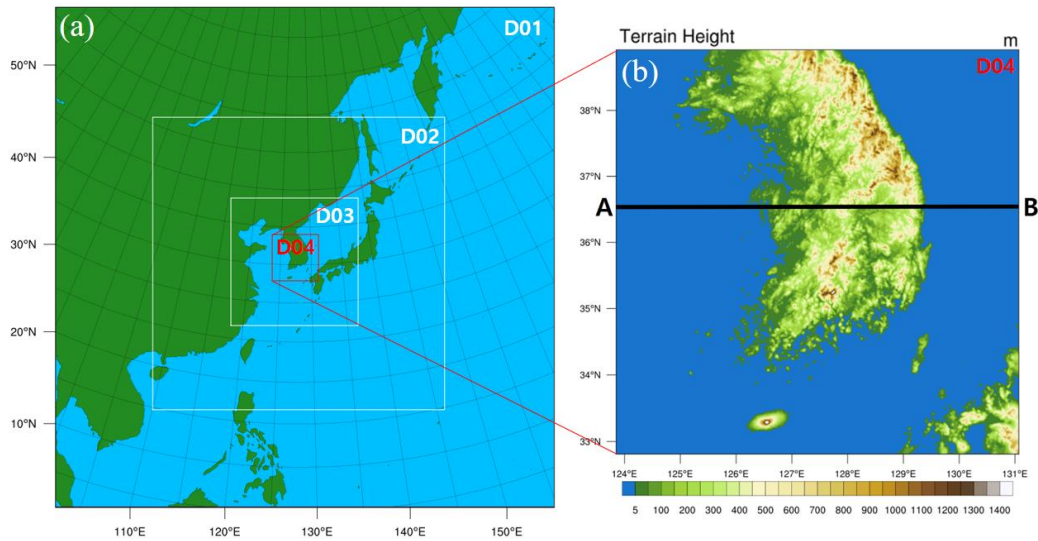
236 The Advanced Research WRF model (Skamarock et al., 2008) Version 4.1 was used in

237 this study, and the initial and boundary conditions were obtained from the $1^\circ \times 1^\circ$ reanalysis data

238 of the National Centers for Environmental Prediction/National Centers for Atmospheric
239 Research (NCEP/NCAR) Final analysis (FNL). The model consisted of four domains with 36 km
240 (201×201), 12 km (352×352), 4 km (460×460), and 1.33 km (201×201) horizontal grid spacings,
241 which included CPS gray-zone resolution (Figure 4a). We used two-way nested domains with a
242 Lambert conformal map projection. The domain contained 32 vertical levels from the surface to
243 the top of the atmosphere at 50 hPa. The model used the WSM6 cloud microphysics scheme
244 (*Hong&Lim, 2006*), the Yonsei University planetary boundary layer scheme (*Noh et al., 2003*;
245 *Hong et al., 2006*), Dudhia short-wave radiation scheme (*Dudhia, 1989*), and long-wave
246 radiation scheme based on the rapid radiative transfer model (*Mlawer et al., 1997*). In this study,
247 the KF scheme and MSKF schemes were selected for the sensitivity experiments. The KF
248 scheme is a sub-grid scheme with deep and shallow convection and uses a mass flux approach to
249 calculate the CAPE-based closure assumption scheme. The MSKF scheme is a scale-aware
250 version of the KF scheme. Compared to the KF, the MSKF includes changes in the convective
251 adjustment timescale and improvements to the entrainment formulations (*Zheng et al., 2016*).
252 The MSKF also incorporates a grid-aware scaling parameter into these modifications. The main
253 advantages of the MSKF scheme are as follows.

254

255



256

257 **Figure 4.** Map showing (a) Four nested domains with 36 km, 12 km, 4 km, and 1.33 km grid
 258 spacing in WRF, and (b) terrain height for the finest domain (red box identified as the D04
 259 domain in Figure 4a). Line AB in Figure 4b marks the vertical cross-section used in Figure 10.

260

261 Both the KF and MSKF schemes remove 90% of the potential energy within the CAPE
 262 timescale period (*Bechtold et al.*, 2001), and the CAPE timescale is limited to 1800 s and 3600 s
 263 in the cloud layer for deep and shallow convections, respectively. The convection time step (τ)
 264 connected to the CAPE timescale of clouds is proportional to the grid length DX (*Fritsch et al.*,
 265 1976; *Fritsch&Chappell*, 1980). The CAPE timescale works to effectively resolve atmospheric
 266 instability at coarse grid resolution. However, the higher model grid resolution leads to an
 267 increase in the unresolved cloud area and faster saturation speed, which causes rapid CAPE
 268 removal problems within the CAPE timescale resulting in intense precipitation. For reduction of
 269 these inadequacies, the MSKF scheme uses the adjustment timescale τ (s) based on *Bechtold et*
 270 *al.* (2008), which is multiplied by the scaling parameter (β) impacted by the horizontal grid-scale
 271 (*Zheng et al.*, 2016).

272 The CAPE adjustment timescale can be estimated as:

$$273 \quad \tau = \frac{H}{(\delta m_b A_e)^{\frac{1}{3}}} \beta, \quad (1)$$

274 where H is cloud depth (m), δm_b is the updraft mass flux of cloud base per unit density
 275 (m s^{-1}), A_e is the potential energy of the saturated air supplied to the cloud base ($\text{m}^2 \text{s}^{-2}$), and β is
 276 the scaling parameter defined as

$$277 \quad \beta = 1 + \ln\left(\frac{25}{DX}\right). \quad (2)$$

278 β is set to approximately 2.8 and 4.2 at 4 and 1 km model grid spacings in equation (2),
 279 respectively. As the grid spacing decreases, the CAPE adjustment timescale using the scale-
 280 aware parameter becomes longer. A longer CAPE timescale allows slower elimination
 281 convective instability.

282 Additionally, the MSKF scheme adjusts the minimum entrainment rate using the scale-
 283 aware parameter similar to the timescale concept. The adjusted entrainment rate is defined as:

$$284 \quad \Delta M_e = M_b \frac{\alpha \beta}{z_{LCL}} \Delta p, \quad (3)$$

285 where M_b is the updraft mass flux per unit area (kg s^{-1}) at the cloud base, β is the scale-
 286 aware parameter (eq. 2), Δp is the pressure depth of a model level (Pa), and Z_{LCL} (m) is the
 287 height of the cloud base. The value of α (0.03) is a constant parameter (*Tokioka et al.*, 1988). The
 288 cloud base height replaces the arbitrarily fixed cloud radius because entrainment is associated
 289 with the sub-cloud layer depth. The mixing rate increases with the β value, limiting the sub-grid
 290 convection (*Lin et al.*, 2013). This adjusted scale-aware entrainment formulation allows the
 291 mixing rate, ΔM_e , to increase with decreasing horizontal grid spacing. At higher resolutions, the
 292 effects of the KF scheme are reduced, which inhibits deep convection.

293 The experiments conducted in this study consist of two parts. In Part 1, three experiments
 294 were conducted to investigate the difference between the KF and MSKF schemes and the impact
 295 of CPS in the gray-zone (KF_D12, KF, and MSKF runs). The KF_D12 run employed the KF
 296 scheme only in D01 and D02 domains with 36 and 12 km resolutions, respectively, while the KF
 297 and MSKF runs used the KF and MSKF schemes in all domains, respectively. In Part 2, we
 298 conducted two additional experiments (CTS and ENT) to investigate the effects of the scale-
 299 aware parameter in the MSKF scheme on the convective activity simulation causing heavy
 300 rainfall. The CTS run is the same as the MSKF run but for the scale-aware parameter value of 1
 301 in the CAPE timescale (i.e., the same CAPE timescale as in the KF scheme), and the ENT run is
 302 identical to the MSKF scheme except for the same entrainment rate as in the KF scheme. As the
 303 horizontal model resolution increases (e.g., D03 or D04 domains), we can examine the effect of
 304 the scale-aware parameter on the reduced (increased) CAPE timescale (entrainment rate) of the
 305 MSKF scheme by comparing the CTS (ENT) and MSKF runs. The experiments conducted in
 306 this study are summarized in Table 1.

307 **Table 1. List of experiments conducted in this study.**

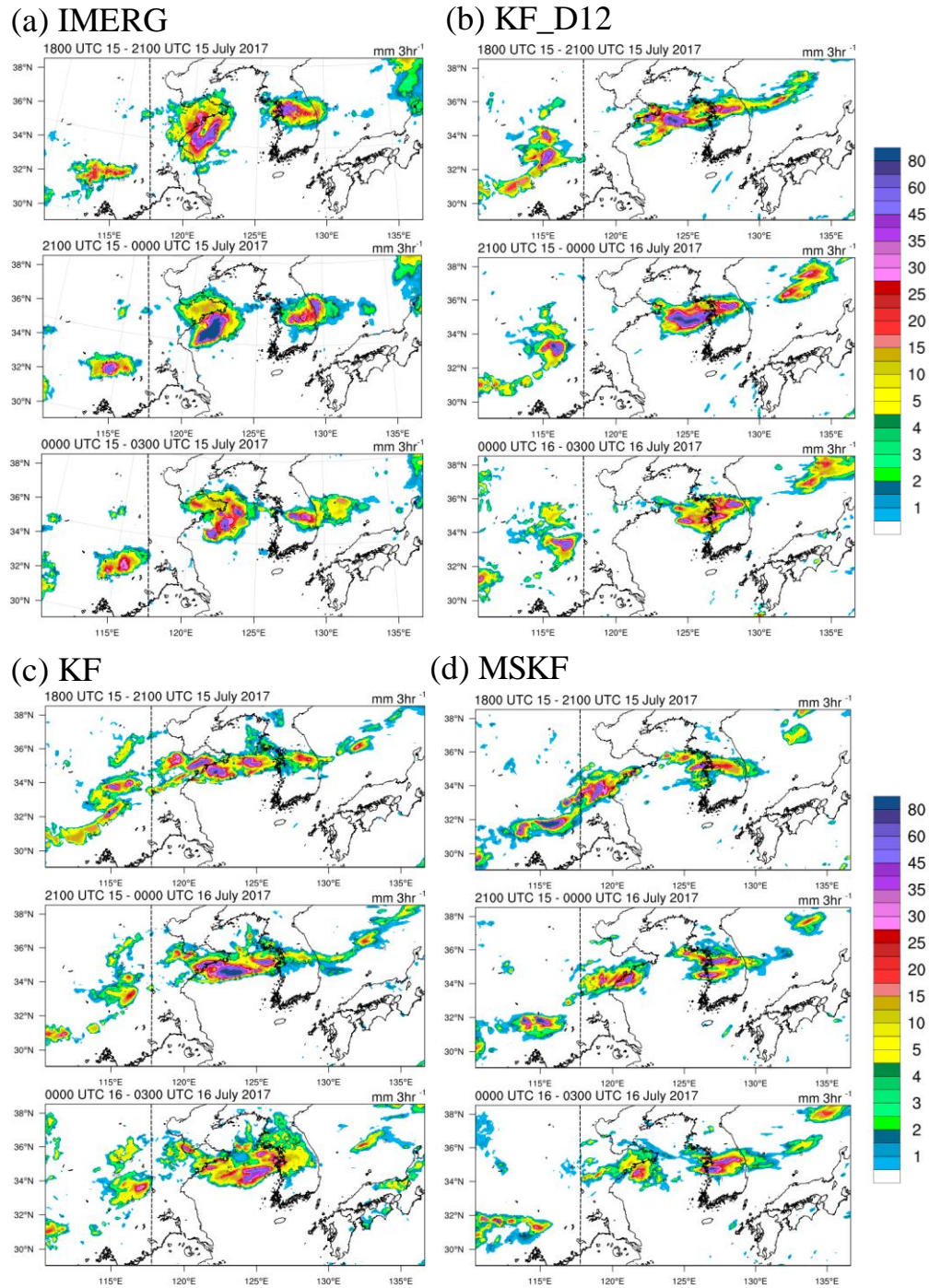
Experiments	Description
KF_D12	KF scheme used only for the D01 and D02 domains
KF	KF scheme used for all domains
MSKF	MSKF scheme used for all domains
CTS	Same as MSKF run, but for the same CAPE timescale as in KF scheme
ENT	Same as MSKF run, but for the same entrainment as in KF scheme

308

309 **3 Results**

310 3.1 Difference between the KF and MSKF schemes and CPS impact on the gray-zone

311 In this section, simulated precipitation from the KF_D12, KF, and MSKF runs was
312 compared with the Integrated Multi-SatellitE Retrievals for Global Precipitation Measurement
313 (IMERG, *Huffman et al.*, 2015a; 2015b) and FNL 0.25° reanalysis data to analyze the differences
314 in rainfall and synoptic fields among the three runs. As mentioned in Figure 3, two types of
315 precipitation zones were observed in Figure 5a. One was the precipitation zone caused by CC1,
316 which started over the Seoul metropolitan region (Gyeonggi-bay) and moved southeastward.
317 Another related to CC2 moved from the Shandong Peninsula to the Yellow Sea. The IMERG
318 satellite image indicates that the precipitation area related to CC1 over Gyeonggi-bay moved
319 southeastward, resulting in heavy rainfalls in Cheong-ju. Figure 5b-d shows the 3-hourly
320 accumulated total (subgrid-scale and grid-scale) precipitation in the D02 domain of three runs. In
321 the KF_D12 run (Figure 5b), CC1 was located over the eastern part of Seoul and was expanded
322 northeastward; the model simulated simply one convective system instead of two convective
323 systems. Furthermore, unreasonable shifting of the simulated precipitation associated with CC2
324 to the Yellow Sea instead of the southern part of the Shandong Peninsula caused an error of
325 overestimated rainfall in the ocean. The KF run (Figure 5c) simulated similar features to the
326 KF_D12 run (i.e., overestimated precipitation over the Gyeonggi-Bay). However, the
327 precipitation core was shifted west in KF run compared to the KF_D12 run. Contrastingly, the
328 MSKF run (Figure 5d) reproduced the spatial pattern of simulated precipitation more correctly
329 relative to KF_D12 and KF runs. Notably, in the MSKF run, CC1 and CC2 were simulated
330 separately, similar to those in the IMERG. Hence, the heavy rainfall related to CC1 was
331 reasonably captured.

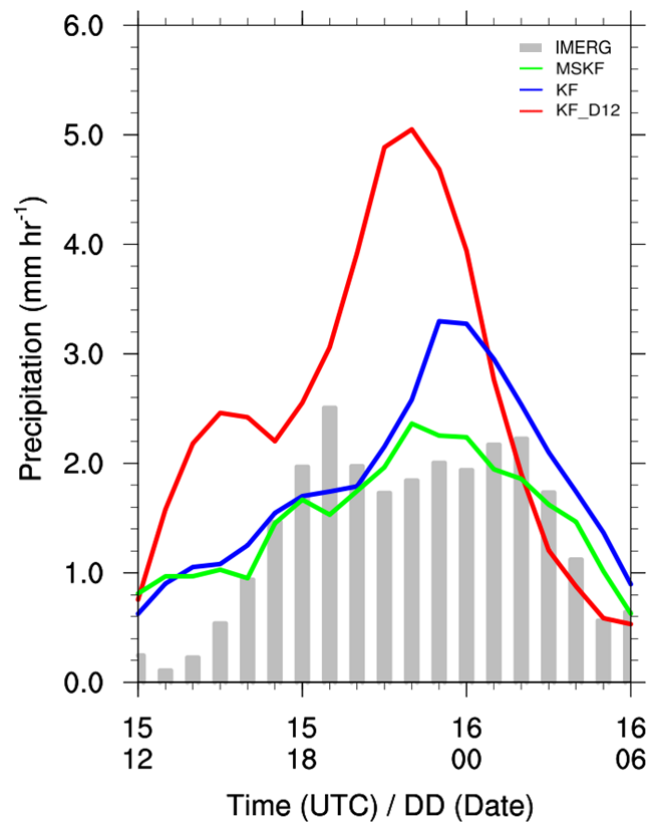


332

333 **Figure 5.** Spatiotemporal images showing three-hourly accumulated total precipitation (mm) in
 334 the D02 domain between 1800 UTC, 15 July and 0300 UTC, 16 July 2017. Black dashed lines
 335 indicate the left boundary of the D03 domain in Figure 3a.

336

337 Figure 6 shows the time series of domain-averaged hourly precipitation for observed
 338 (IMERG) and simulated precipitation (i.e., the D02 domain) averaged for the target region,
 339 including the Korean Peninsula and the Yellow Sea. Heavy precipitation was observed for 18
 340 hours (1200 UTC, 15 July to 0300 UTC, 16 July), with two peaks at 1800 UTC 15 and 0300
 341 UTC 16. However, the KF_D12 run reproduced the two heavy precipitation peaks earlier than in
 342 the observation with the overestimated precipitation due to unreasonable simulation in the
 343 Yellow Sea. The simulated precipitation of the KF run is more reasonable than the KF_D12 run.
 344 However, the precipitation in the target region was still overestimated than IMERG.
 345 Contrastingly, the MSKF run simulated heavy precipitation most reasonably in the target region
 346 in terms of amount.



347

348 **Figure 6.** Graph depicting time-series of hourly accumulated rainfall averaged between 36-
 349 38 °N and 123-130 °E for the IMERG (gray box), KF_D12 (red line), KF (blue line), and MSKF

350 (green line) run. Simulated precipitation is calculated from the results of the 4-km resolution
 351 domain.

352

353 To quantitatively evaluate the performance of the heavy precipitation simulation (Figure
 354 7), we calculated two standard skill scores (i.e., the treat score (TS) and bias score (BS)) for
 355 precipitation with various precipitation intensity thresholds (e.g., 0.5, 5, 10, 20, 30, 40, and 50
 356 mm). Two scores were calculated using the following equations (Eq. 4 and 5) (Wilks, 2011). As
 357 BS and TS approach 1, the accuracy of the model in forecasting rainfall events increases.

358

$$359 \quad BS = \frac{Hits + False\ alarms}{Hits + Misses}, \text{ and} \quad (4)$$

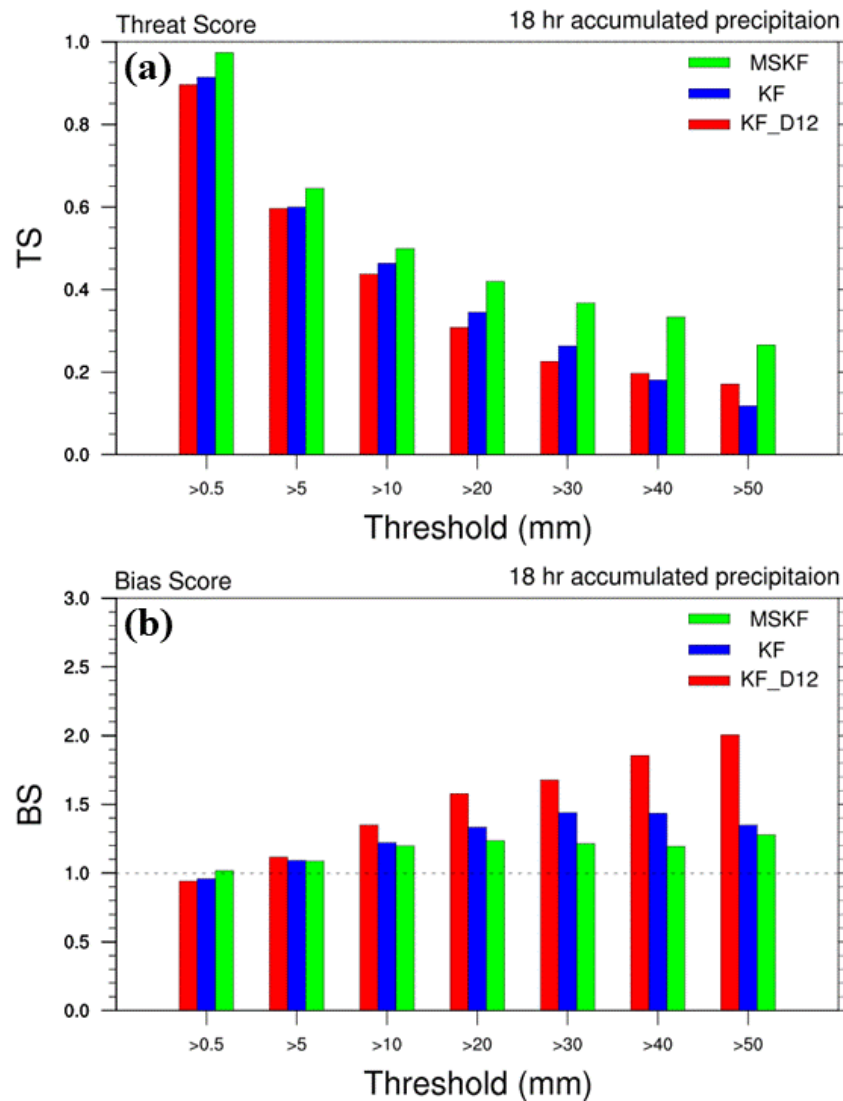
$$360 \quad TS = \frac{Hits}{Hits + False\ alarms + Misses}. \quad (5)$$

361

362 The precipitation detection skills (e.g., BS and TS) decreased as the threshold increased
 363 in the three runs (Figure 7). The TS for the precipitation forecast is the highest in the MSKF run
 364 compared to the other runs (e.g., the KF_D12 and KF runs) for all the considered precipitation
 365 thresholds. In the TS, the KF and KF_D12 runs have a low score than the MSKF run across the
 366 entire range of precipitation intensity thresholds. The result of the BS indicates that the KF and
 367 KF_D12 runs simulated more ‘false alarms’ and ‘misses’ than ‘hits’ compared to those of the
 368 MSKF run. In the BS, the MSKF run has high model performance in detecting precipitation
 369 across the entire range of precipitation intensities by maintaining the BS value of around 1.
 370 However, the BS in the KF and KF_D12 runs increases more significantly than in the MSKF
 371 run. Notably, the BS in the KF_D12 run increases dramatically as the threshold increases,
 372 suggesting that in the low performance of the KF_D12 run, the number of falsely classified grid

373 boxes as ‘false alarms’ tends to be substantially larger than the number of incorrectly classified
 374 grid boxes as ‘misses’. The KF_D12 run has many ‘false alarms’ due to excessive precipitation
 375 in the Yellow Sea before entering the Koran Peninsula. In the KF and KF_D12 runs, as a result,
 376 the overall forecasting abilities of the precipitation products in capturing the correct magnitude
 377 of intense precipitation are less accurate than that in the MSKF run.

378



379

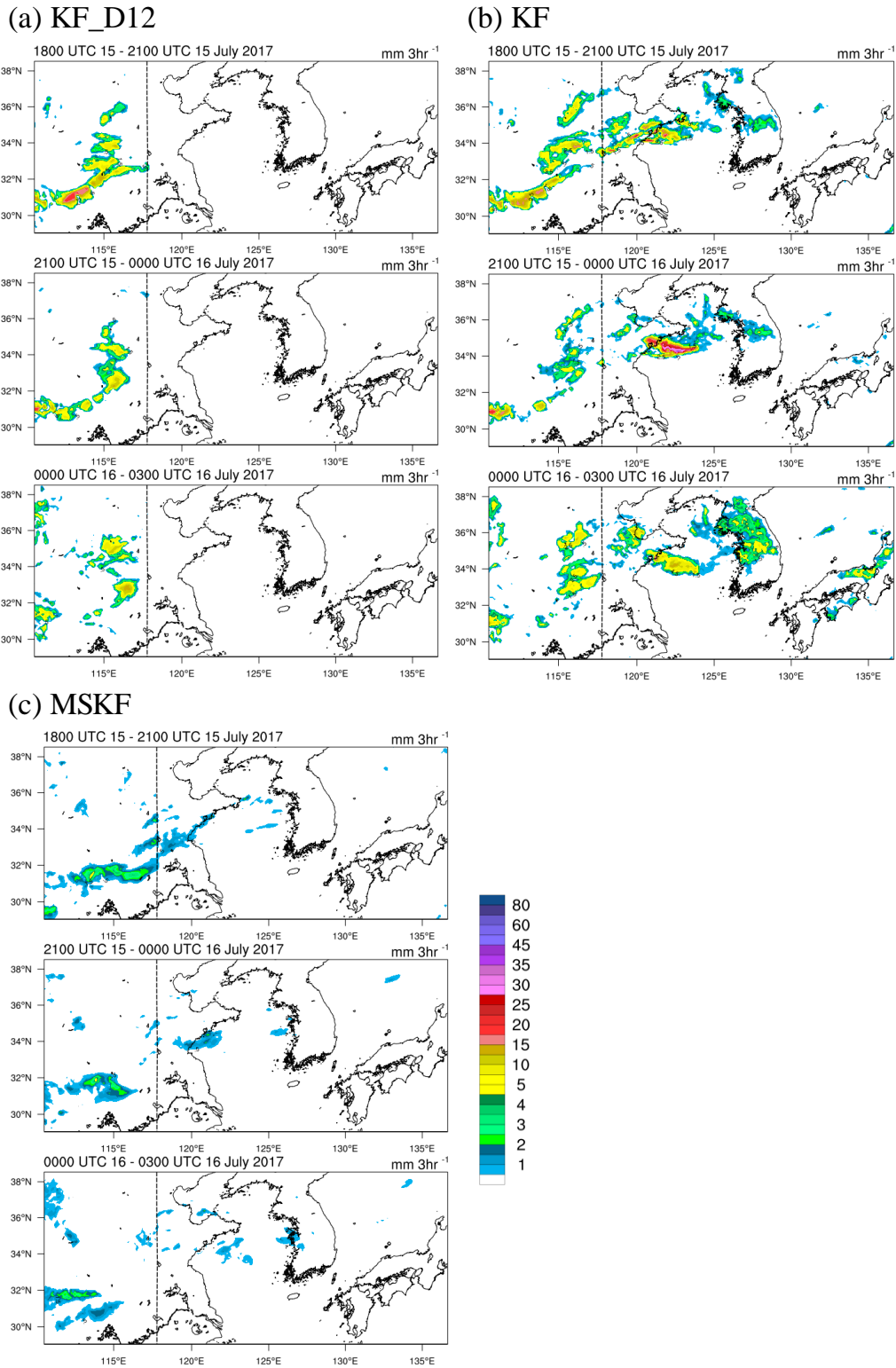
380

381 **Figure 7.** Bar plots of the statistical indices corresponding to the KF_D12, KF, and MSKF runs
 382 with IMERG based on different thresholds of 18-hourly accumulated precipitation (from 1200

383 UTC, 15 July to 0600 UTC, 16 July 2017). The simulated precipitation is interpolated to the
384 observation grid points, and model statistics are calculated for South Korea and the Yellow Sea
385 (between 36-38 °N and 123-130 °E).

386

387 Figure 8 shows the distribution of subgrid-scale precipitation simulated by the CPS. The
388 KF run simulated subgrid-scale precipitation is similar to the KF_D12 run in the D02 domain
389 outside the D03 domain. However, within the D03 domain, only the KF run simulated subgrid-
390 scale precipitation employing CPS for the domain. The KF_D12 run could not produce subgrid-
391 scale precipitation because of the absence of CPS in the D03 domain. Contrastingly, the subgrid-
392 scale precipitation simulated in both the D02 and D03 domains of the MSKF run was reduced
393 compared with that in the KF run. The MSKF scheme simulates a smaller ratio of subgrid-scale
394 precipitation to total precipitation than in the KF scheme as the horizontal resolution increases
395 because the scale-aware parameter in the MSKF scheme smoothly decreases the role of CPS and
396 increases the removal of atmospheric instability by MPS.



397

398 **Figure 8.** Spatiotemporal images (similar to Figure 5) for three-hourly accumulated subgrid-
 399 scale precipitation (mm).

400

401 To investigate the causes of the different simulations among the three runs, we analyzed
402 the synoptic conditions from the reanalysis and simulations of the D02 domain in Figure 9. In FNL
403 (Figure 9a), LLJ ($> 13 \text{ m s}^{-1}$) transporting wet and warm air was located in two regions (e.g., the
404 Shandong and Korean Peninsulas) with heavy precipitation. (see Figure 5a). The three WRF runs
405 reproduced wet and warm air transport by LLJ from inland China to the Korean Peninsula.
406 However, the LLJ cores were inappropriately located in inland China and the Yellow Sea in the
407 KF_D12 and KF runs (Figure 9b, c), and the intensity of LLJ was overestimated, which induced
408 enhanced moisture transport. Notably, LLJs located at the Shandong Peninsula in the reanalysis
409 were further shifted to the Yellow Sea in the KF_D12 run. Additionally, low-pressure systems at
410 700 hPa unrealistically developed in the LLJ cores in the KF_D12 and KF runs. More moisture
411 transported by the enhanced LLJ led to increased convective instability over the regions, which
412 developed convective activities and low-level pressure erroneously. Contrarily, the MSKF run
413 reproduced the low-pressure system and LLJ similar to the reanalysis regarding location and
414 intensity.

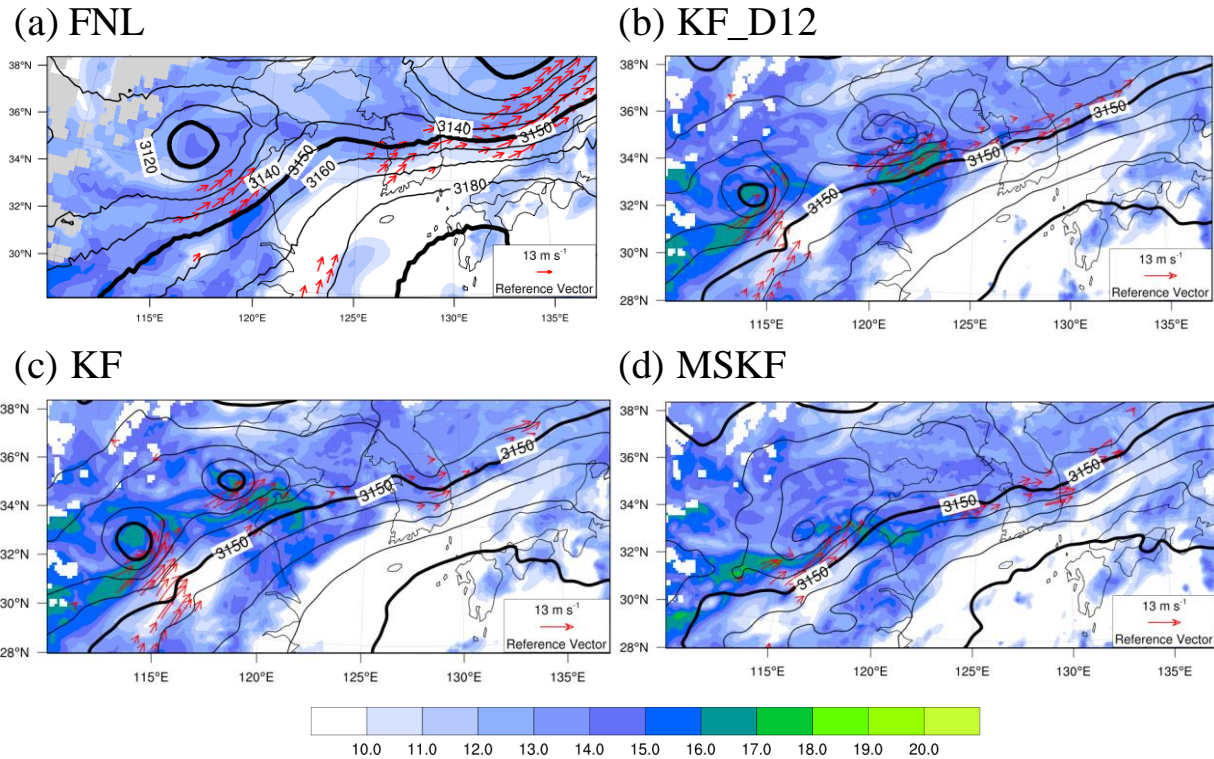
415

416

417

418

419



420

421 **Figure. 9.** Spatial contour maps of the wind ($>13 \text{ m s}^{-1}$, red vector), and water vapor (g kg^{-1} ,
 422 shaded) at 850 hPa, and geopotential height (m, black lines) at 700 hPa in the D02 domain at
 423 1800 UTC, 15 and 0000 UTC, 16 July 2017.

424

425 The locations of LLJ cores were consistent with those of the heavy precipitation area in
 426 the three runs, implying that LLJ played a significant role in the development of heavy
 427 precipitation by transporting wet and warm air from the subtropics. While the KF_D12 run only
 428 eliminated atmospheric instability by MPS in the D03 and D04 domains, the MPS could not
 429 adequately trigger convection over the Shandong Peninsula. The MPS unreasonably removed the
 430 atmospheric instability in the Yellow Sea rather than the peninsula. Additionally, the MPS
 431 prominently overestimated convection in the Yellow Sea, further increasing heavy precipitation
 432 in the region by enhancing LLJ and moisture convergence. Contrarily, subgrid-scale
 433 precipitation in the Shandong Peninsula in the KF run implied that convection was developed in

434 the proper location. However, the action of CPS was excessive, which led to the distortion of
435 synoptic fields such as intensified LLJs and increased moisture convergence in the Shandong
436 Peninsula and the Yellow Sea. Thereby, MPS also simulated considerable grid-scale
437 precipitation in the regions, indicating unreasonable overestimation of total precipitation by CPS
438 and MPS. However, in the MSKF run, subgrid-scale precipitation was decreased due to
439 decreasing role of CPS compared with that in the KF run. Therefore, similar to the IMERG, the
440 MSKF run reasonably captured torrential rainfall over the Shandong Peninsula associated with
441 CC2 and heavy precipitation in the Korean Peninsula related to CC1.

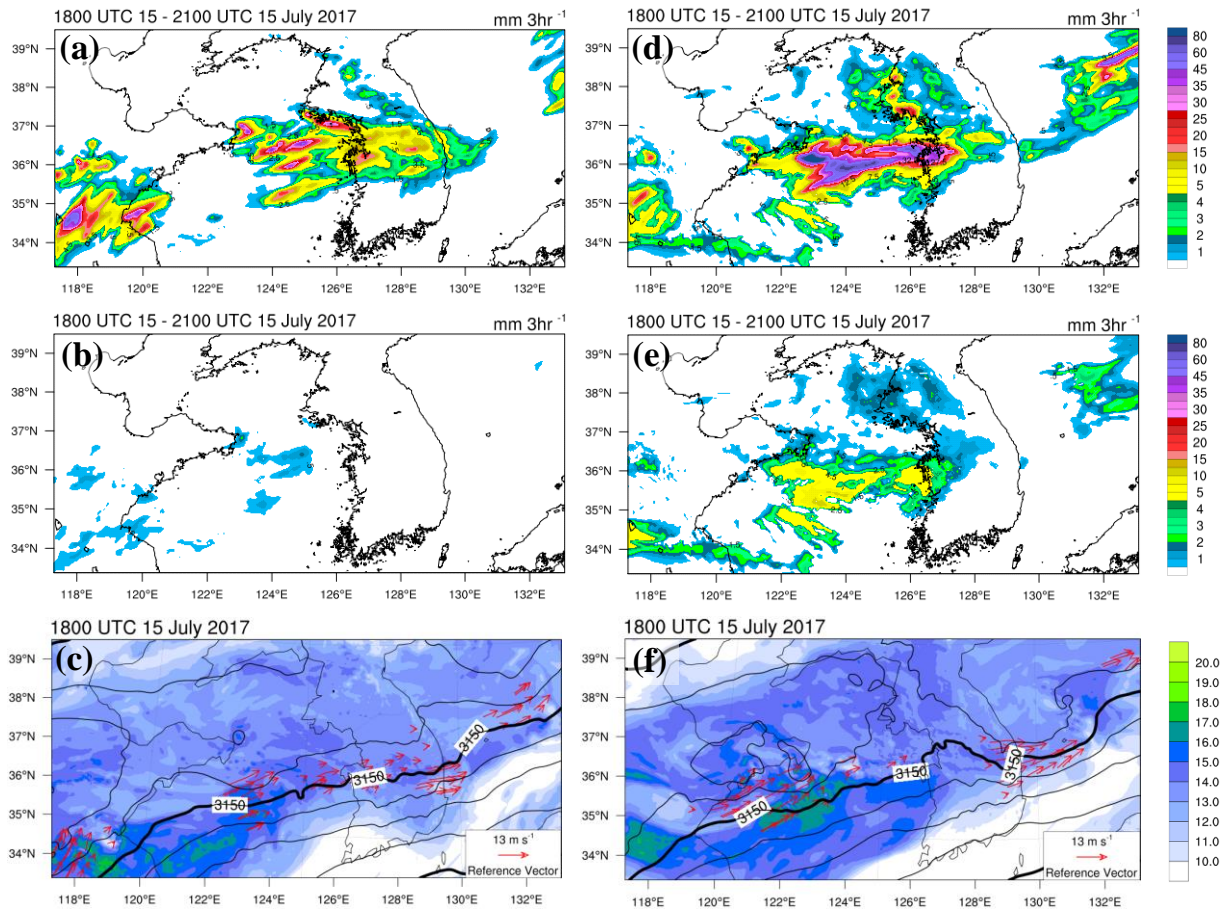
442 These results imply that high-resolution simulation of convective activities by MPS alone
443 could lead to inappropriate overestimation of precipitation, as atmospheric instability may not be
444 adequately reduced. Furthermore, CPS without scale-awareness may lead to the erroneous
445 simulation of heavy precipitation at high resolution due to the exaggeration of convection and
446 distortion of the synoptic fields. Therefore, the simulation of heavy precipitation using a high-
447 resolution model would require a scale-aware CPS.

448 3.2. Sensitivity run results for rainfall and synoptic environment

449 The previous section showed that the MSKF run improved the heavy precipitation
450 simulation in the Cheong-ju region compared to the KF_D12 and KF runs; because the MSKF
451 scheme represents an incorporative transition from the CPS-induced precipitation to MPS-
452 induced precipitation in the gray-zone. To investigate the reason for the improved simulation of
453 heavy precipitation in the MSKF run, we conducted two additional sensitivity experiments on the
454 scale-aware parameter of the MSKF scheme: (1) the CTS run, which modified the CAPE
455 timescale, and (2) the ENT run, which changed the entrainment rate.

456 Figure 10 shows the simulated total precipitation, subgrid-scale precipitation, and
457 synoptic fields reproduced by CTS and ENT runs. In Figure 10a, the CTS run captured the heavy
458 precipitation zones related to CC1 and CC2, similar to the MSKF run (see top panel of Figure
459 5d). However, the simulated precipitation zone in the Yellow Sea caused by CC1 was further
460 shifted westward, and subgrid-scale precipitation was simulated marginally more in the Yellow
461 Sea than in the MSKF run (Figure 10b), suggesting that the reduced CAPE timescale of the CTS
462 run compared to that of the MSKF run led to the faster removal of the atmospheric instability.
463 The reduced CAPE timescale of the CTS run resulted in the rapid development of convective
464 activities in the Yellow Sea rather than the Korean Peninsula (Figure 10b), which unreasonably
465 enhanced moisture convergence and LLJ at 850 hPa (Figure 10c). Thus, the CTS run simulated
466 grid-scale precipitation in the Yellow Sea earlier than in the MSKF run and corresponding
467 observation due to the distorted synoptic conditions. Contrastingly, the ENT run (Figure 10d)
468 unrealistically simulated the merged precipitation zone in the Yellow Sea, which is similar to the
469 KF run (Figure 5c). Compared to the CTS and MSKF runs, the ENT run tends to overestimate
470 subgrid-scale precipitation in the Yellow Sea because the entrainment rate was relatively weak
471 due to the absence of scale-aware parameters (Figure 10e). Therefore, the ENT run simulated
472 enhanced convective activities and excessive sub-grid precipitation in the Yellow Sea by CPS.
473 Furthermore, the enhanced convective activities led to the distortion of synoptic fields, such as
474 intensified LLJ and the exaggerated moisture convergence, which caused excessive grid-scale
475 precipitation in the Yellow Sea (Figure 10f). Therefore, the MSKF scheme could improve heavy
476 precipitation because of increasing CAPE timescale and enhanced entrainment process, which
477 led to modulating atmospheric instability. In other words, the subgrid-scale (grid-scale)
478 precipitation by the CPS (MPS) smoothly decreased (increase) in the MSKF run as the horizontal

479 resolution increased within the gray zone. The ENT run had a more significant error in simulated
 480 precipitation than in the CTS run, indicating that the enhanced entrainment rate of the MSKF
 481 scheme contributed more than the increased CAPE timescale to the improved simulation of
 482 heavy precipitation.



483

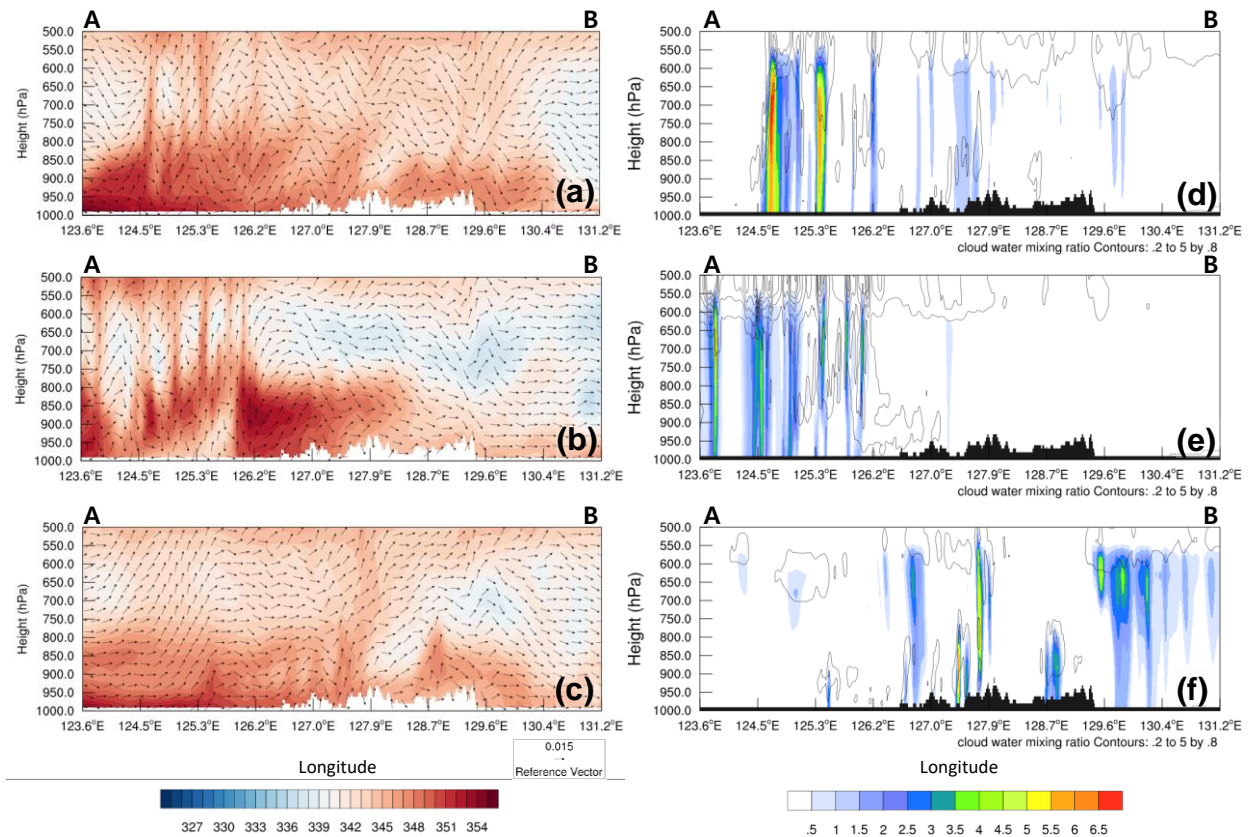
484 **Figure 10.** Spatiotemporal maps of the (a, d) total precipitation (mm) and (b, e) convective
 485 precipitation (mm) between 1800 and 2100 UTC, 15 July 2017 (c, f) 850 hPa wind (m s⁻¹, red
 486 vector) and water vapor (g kg⁻¹, shaded), and 700 hPa geopotential height (m, black lines) at
 487 1800 UTC, 15 July 2017, in the D03 domains of the CTS (left panels) and the ENT runs (right
 488 panels).

489

490 To investigate the effect of scale-aware parameters on convective development, in Figure
491 11, we examined the vertical fields across the region where the difference in precipitation was
492 prominent between the sensitivity runs (see solid line in Figure 4b). The D04 domain results
493 were used to analyze the small-scale features, and the analysis time was 2100 UTC on 15 July ,
494 which was an appropriate time to examine the effects of the scale-aware parameter. Figure 11
495 shows a notable difference in the vertical distribution of the equivalent potential temperature
496 (EPT) as compared to those of the other experiments from the Yellow Sea (123.6 °E) to the
497 Cheong-ju region (127.9 °E). The CTS run simulated high EPT at the low-level in the Yellow
498 Sea, which increased atmospheric instability and then unreasonably developed intense
499 convective activities between 124.5 - 125.5 °E (Figure 11a). As shown in Figure 10b, the shorter
500 CAPE timescale in the CTS run than in the MSKF run triggered convection earlier in the Yellow
501 Sea rather than in the west coast of the Korean Peninsula. The earlier developed convection in
502 the Yellow Sea enhanced LLJ and moisture convergence, resulting in an increase in atmospheric
503 hydrometeors, which could cause excessive grid-scale precipitation (Figure 11d). Also,
504 convection was not prominently simulated in the inland of the Korean Peninsula, and relatively
505 fewer hydrometeors were resolved. Hence, torrential precipitation in Cheong-ju was not sensibly
506 captured (see Figure 10a). Similarly, the ENT run also simulated high EPT at the low-level. The
507 entrainment process, which mixed moist and warm air within convective clouds with dry and
508 cold environment air, was not strengthened because of the absence of a scale-aware parameter
509 (Figure 11b). High EPT led to an unstable atmosphere and overestimated convective
510 precipitation in the Yellow Sea, as shown in Figure 10b. The distorted LLJ and water vapor
511 convergence, resulting in increased atmospheric hydrometeors and then overestimated grid-scale
512 precipitation in most of the Yellow Sea regions. Since most hydrometeors were converted to

513 grid-scale precipitation in the Yellow Sea (Figure 11e), precipitation in the inland of the Korean
 514 Peninsula was considerably less, as shown in Figure 10d. On the other hand, the MSKF run
 515 realistically simulated low-level EPT, atmospheric stability, and hydrometeors in the Yellow Sea
 516 (Figure 11c and f). Therefore, it reproduced strong convection and more hydrometeors over the
 517 Cheong-ju region (127.9 °E), which resulted in a reasonable simulation of heavy precipitation by
 518 the CPS and MPS.

519



520

521 **Figure. 11.** Plots of the vertical cross-sections (AB in Figure 3b) of (a-c) equivalent potential
 522 temperature (K, shaded) and wind (m s^{-1} , vector), and (d-f) cloud hydrometeors mixing ratio (g
 523 kg^{-1} , shaded) and rain water mixing ratio (g kg^{-1} , contour) at 2100 UTC, 15 July 2017. Upper,
 524 middle, and lower panels indicate the CTS, ENT, and MSKF runs, respectively. Cloud
 525 hydrometeors are calculated by the summation of cloud water, ice, snow, and graupel.

526

527 **4 Conclusion**

528 This study investigated the impact of the scale-aware CPS across the gray-zone in the
529 WRF model on a heavy precipitation event over the Korean Peninsula. We selected the KF and
530 MSKF schemes as non-scale-aware CPS and scale-aware CPS, respectively. The MSKF scheme
531 uses a scale-aware parameter modifying the CAPE timescale and the entrainment process of the
532 KF scheme as a function of the horizontal grid spacing. The multi-nesting method is employed
533 with four domains with 36, 12, 4, and 1.33 km horizontal resolutions to consider the gray-zone
534 resolution.

535 According to our results, the KF runs (i.e., KF_D12 and KF runs) unreasonably
536 overestimated precipitation in the Yellow Sea and distorted synoptic fields such as LLJs and
537 moisture convergence. In the KF_D12 run, only the MPS resolved convective activities for the
538 domains with high-resolution (i.e., 4 and 1.33 km) and overestimated grid-scale precipitation in
539 the Yellow Sea because atmospheric instability is inadequately reduced. The CPS without scale-
540 awareness (i.e., KF run) also caused the erroneous precipitation simulation due to the
541 exaggeration of convection and distortion of the synoptic fields. Contrastingly, the MSKF run
542 realistically simulated precipitation and synoptic fields. And, the sensitivity experiments for the
543 scale-aware parameter (i.e., CTS and ENT runs) showed that the shorter CAPE timescale and
544 decreased entrainment process of the KF scheme compared with those of the MSKF scheme led
545 to the unreasonable fast development and exaggeration of convective activities, respectively.
546 Additionally, the ENT run has a more significant error in simulated precipitation than the CTS
547 run, suggesting that the enhanced entrainment process of the MSKF scheme contributes more to
548 the improved simulation of heavy precipitation than the increased CAPE timescale.
549 Consequently, the MSKF scheme with a scale-aware parameter realistically simulated

550 precipitation and synoptic fields by decreasing the subgrid-scale convection by the CPS and
551 increasing the grid-scale convection by MPS as the horizontal resolution increases.

552 As the horizontal resolution of numerical models for weather forecasting has increased
553 due to the remarkable advances in computing resources, more realistic grid-scale simulations are
554 required. Studies have shown that (*Jeworrek et al.*, 2019; *Hong&Dudhia*, 2012) scale-aware
555 physics schemes can improve the high-impact weather simulation when using very high-
556 resolution numerical models. This study also improved the understanding of the scale-aware CPS
557 role in heavy precipitation simulation at high-resolution. However, this study has some
558 limitations. Only the KF-based CPSs in the WRF model and a heavy rainfall case in the Korean
559 Peninsula are tested. Therefore, further experiments for the various scale-aware CPSs (e.g.,
560 scale-aware Grell-Freitas (*Grell&Freitas*, 2014) and gray-zone simplified Arakawa-Schubert
561 (*Kwon&Hong*, 2017)) should be conducted for more heavy precipitation. We could also plan
562 sensitivity tests using various combinations of the scale-aware CPSs and MPSs because the
563 predictability of convective systems associated with heavy rainfall can depend on these
564 combinations.

565 **Acknowledgments**

566 This work was partially funded by the 2020 Republic of Korea Airforce Numerical Weather
 567 Prediction Research and Development Program, the development of Numerical Weather
 568 Prediction and Data Application Techniques, and the Ulsan National Institute of Science and
 569 Technology [Grant No. 1.210045.01].

570

571 **Data Availability Statement**

572 The National Centers for Environmental Prediction Global Final Analysis (NCEP-FNL) data
 573 are available online (<https://rda.ucar.edu/datasets/ds083.2/> and
 574 <https://rda.ucar.edu/datasets/ds083.3/>). IMERG was provided by the NASA Goddard Space
 575 Flight Center's IMERG and PPS teams, which develop and compute IMERG as a contribution
 576 to the GPM mission, and archived at the NASA GES DISC
 577 (https://disc.gsfc.nasa.gov/datasets/GPM_3IMERGHH_V06/summary) and online
 578 (<https://gpm.nasa.gov/data/directory>).

579

580 **Reference**

581 Alapaty, K., Herwehe, J. A., Otte, T. L., Nolte, C. G., Bullock, O. R., Mallard, M. S., Kain, J. S., and Dudhia, J.
 582 (2012), Introducing subgrid-scale cloud feedbacks to radiation for regional meteorological and climate modeling,
 583 *39*(24), doi:<https://doi.org/10.1029/2012GL054031>.
 584 Arakawa, A., Jung, J.-H., and Wu, C.-M. J. M. m. (2016), Multiscale modeling of the moist-convective atmosphere,
 585 *56*, 16.11-16.17.
 586 Arakawa, A., Jung, J. H., and Wu, C. M. (2011), Toward unification of the multiscale modeling of the atmosphere,
 587 *Atmos. Chem. Phys.*, *11*(8), 3731-3742, doi:10.5194/acp-11-3731-2011.
 588 Bechtold, P., Bazile, E., Guichard, F., Mascart, P., and Richard, E. J. Q. J. o. t. R. M. S. (2001), A mass-flux
 589 convection scheme for regional and global models, *127*(573), 869-886.
 590 Bechtold, P., Koehler, M., Jung, T., Doblas-Reyes, F., Leutbecher, M., Rodwell, M. J., Vitart, F., Balsamo, G. J. Q.
 591 J. o. t. R. M. S. A. j. o. t. a. s., applied meteorology, and oceanography, p. (2008), *Advances in simulating*
 592 *atmospheric variability with the ECMWF model: From synoptic to decadal time-scales*, *134*(634), 1337-1351.
 593 Bechtold, P., Semane, N., Lopez, P., Chaboureaud, J.-P., Beljaars, A., and Bormann, N. J. J. o. A. S. (2014),
 594 Representing equilibrium and nonequilibrium convection in large-scale models, *71*(2), 734-753.
 595 Bengtsson, L., and Körnich, H. (2016), Impact of a stochastic parametrization of cumulus convection, using cellular
 596 automata, in a mesoscale ensemble prediction system, *142*, 1150-1159.

- 597 Charles, M. E., Colle, B. A. J. W., and forecasting (2009), Verification of extratropical cyclones within the NCEP
598 operational models. Part I: Analysis errors and short-term NAM and GFS forecasts, *24*(5), 1173-1190.
- 599 Cho, N.-S., and Lee, T.-Y. J. A.-P. J. o. A. S. (2006), A numerical study of multiple convection bands over the
600 Korean peninsula, *42*(2), 87-105.
- 601 Choi, G., Kwon, W.-T., Boo, K.-O., and Cha, Y.-M. J. et al. (2008), Recent spatial and temporal changes in means
602 and extreme events of temperature and precipitation across the Republic of Korea, *43*(5), 681-700.
- 603 Choi, Y., Lee, H., and Kwon, J. J. T. g. j. o. K. (2013), Recent change on frequency-magnitude of summer extreme
604 rainfall events over the Republic of Korea, *47*(1), 83-97.
- 605 Chung, Y., Kim, H. J. A. Q., Atmosphere, and Health (2019), Observations on changes in Korean Changma rain
606 associated with climate warming in 2017 and 2018, *12*(2), 197-215.
- 607 Davies, T., Cullen, M. J., Malcolm, A. J., Mawson, M., Staniforth, A., White, A., Wood, N. J. Q. J. o. t. R. M. S. A.
608 j. o. t. a. s., applied meteorology, and oceanography, p. (2005), A new dynamical core for the Met Office's global
609 and regional modelling of the atmosphere, *131*(608), 1759-1782.
- 610 Deng, A., Stauffer, D. R. J. J. o. a. m., and climatology (2006), On improving 4-km mesoscale model simulations,
611 *45*(3), 361-381.
- 612 Dudhia, J. J. J. o. t. a. s. (1989), Numerical study of convection observed during the winter monsoon experiment
613 using a mesoscale two-dimensional model, *46*(20), 3077-3107.
- 614 Dudhia, J. J. O. T. (2005), Chapter 8: Part II: Physics Options in MM5.
- 615 Emanuel, K. A., and Raymond, D. J. (1993), THE REPRESENTATION OF CUMULUS CONVECTION IN
616 NUMERICAL MODELS %J Meteorological Monographs, *24*(46), 1-246, doi:10.1175/0065-9401-24.46.1.
- 617 Freitas, S. R., Grell, G. A., Molod, A., Thompson, M. A., Putman, W. M., Santos e Silva, C. M., and Souza, E. P.
618 (2018), Assessing the Grell-Freitas Convection Parameterization in the NASA GEOS Modeling System, *10*(6),
619 1266-1289, doi:<https://doi.org/10.1029/2017MS001251>.
- 620 Fritsch, J. M., and Chappell, C. F. (1980), Numerical Prediction of Convectively Driven Mesoscale Pressure
621 Systems. Part I: Convective Parameterization %J Journal of Atmospheric Sciences, *37*(8), 1722-1733,
622 doi:10.1175/1520-0469(1980)037<1722:Npocdm>2.0.Co;2.
- 623 Fritsch, M. J., Chappell, C. F., and Hoxit, L. R. (1976), The Use of Large-Scale Budgets for Convective
624 Parameterization %J Monthly Weather Review, *104*(11), 1408-1418, doi:10.1175/1520-
625 0493(1976)104<1408:Tuolsb>2.0.Co;2.
- 626 Gerard, L. J. Q. J. o. t. R. M. S. A. j. o. t. a. s., applied meteorology, and oceanography, p. (2007), An integrated
627 package for subgrid convection, clouds and precipitation compatible with meso-gamma scales, *133*(624), 711-730.
- 628 Grell, G. A., and Freitas, S. R. J. A. C. (2014), A scale and aerosol aware stochastic convective parameterization for
629 weather and air quality modeling, %J *Atmospheric Chemistry*
630 *Physics*, *14*(10), 5233-5250.
- 631 Gustafson, J. W. I., Ma, P. L., Xiao, H., Singh, B., Rasch, P. J., and Fast, J. D. J. J. o. G. R. A. (2013), The Separate
632 Physics and Dynamics Experiment (SPADE) framework for determining resolution awareness: A case study of
633 microphysics, *118*(16), 9258-9276.
- 634 Ha, K.-J., Park, S.-K., and Kim, K.-Y. (2005), On interannual characteristics of Climate Prediction Center merged
635 analysis precipitation over the Korean peninsula during the summer monsoon season, *25*(1), 99-116,
636 doi:<https://doi.org/10.1002/joc.1116>.
- 637 Han, J., Pan, H.-L. J. W., and Forecasting (2011), Revision of convection and vertical diffusion schemes in the
638 NCEP Global Forecast System, *26*(4), 520-533.
- 639 Ho, C.-H., and Kang, I.-S. J. J. K. M. S. (1988), The variability of precipitation in Korea, *24*(1), 38-48.
- 640 Ho, C. H., Lee, J. Y., Ahn, M. H., and Lee, H. S. (2003), A sudden change in summer rainfall characteristics in
641 Korea during the late 1970s, *Int J Climatol*, *23*(1), 117-128, doi:10.1002/joc.864.
- 642 Hong, S.-Y., and Dudhia, J. (2012), Next-Generation Numerical Weather Prediction: Bridging Parameterization,
643 Explicit Clouds, and Large Eddies %J Bulletin of the American Meteorological Society, *93*(1), ES6-ES9,
644 doi:10.1175/2011bams3224.1.
- 645 Hong, S.-Y., and Lee, J.-W. J. A. R. (2009), Assessment of the WRF model in reproducing a flash-flood heavy
646 rainfall event over Korea, *93*(4), 818-831.
- 647 Hong, S.-Y., and Lim, J.-O. J. J. A.-P. J. o. A. S. (2006), The WRF single-moment 6-class microphysics scheme
648 (WSM6), *42*(2), 129-151.
- 649 Hong, S.-Y., Noh, Y., and Dudhia, J. (2006), A New Vertical Diffusion Package with an Explicit Treatment of
650 Entrainment Processes %J Monthly Weather Review, *134*(9), 2318-2341, doi:10.1175/mwr3199.1.
- 651 Huffman, G. J., Bolvin, D. T., Braithwaite, D., Hsu, K., Joyce, R., Xie, P., and Yoo, S.-H. J. A. T. B. D. V. (2015a),
652 NASA global precipitation measurement (GPM) integrated multi-satellite retrievals for GPM (IMERG), *4*, 26.

- 653 Huffman, G. J., Bolvin, D. T., Nelkin, E. J., and Tan, J. J. N. G. C. (2015b), Integrated Multi-satellite Retrievals for
654 GPM (IMERG) technical documentation, *612*(47), 2019.
- 655 Jankov, I., Schultz, P. J., Anderson, C. J., and Koch, S. E. J. J. o. H. (2007), The impact of different physical
656 parameterizations and their interactions on cold season QPF in the American River basin, *8*(5), 1141-1151.
- 657 Jeworrek, J., West, G., and Stull, R. (2019), Evaluation of Cumulus and Microphysics Parameterizations in WRF
658 across the Convective Gray Zone %J Weather and Forecasting, *34*(4), 1097-1115, doi:10.1175/waf-d-18-0178.1.
- 659 Kain, J. S. J. J. o. a. m. (2004), The Kain–Fritsch convective parameterization: an update, *43*(1), 170-181.
- 660 Kang, I.-S., Ho, C.-H., and Min, K.-D. J. J. o. K. M. S. (1992), Long-range forecast of summer precipitation in
661 Korea, *28*(3), 283-292.
- 662 Khairoutdinov, M., and Randall, D. J. J. o. A. S. (2006), High-resolution simulation of shallow-to-deep convection
663 transition over land, *63*(12), 3421-3436.
- 664 Kim, C., Seo, M.-S., and Atmosphere, k. J. (2008), Change-Point in the Recent (1976-2005) Precipitation over
665 South Korea, *18*(2), 113-122.
- 666 Kuang, Z., and Bretherton, C. S. J. J. o. t. A. S. (2006), A mass-flux scheme view of a high-resolution simulation of
667 a transition from shallow to deep cumulus convection, *63*(7), 1895-1909.
- 668 Kwon, M., Jhun, J.-G., and Ha, K.-J. (2007), Decadal change in east Asian summer monsoon circulation in the mid-
669 1990s, *34*(21), doi:<https://doi.org/10.1029/2007GL031977>.
- 670 Kwon, Y. C., and Hong, S.-Y. (2017), A Mass-Flux Cumulus Parameterization Scheme across Gray-Zone
671 Resolutions %J Monthly Weather Review, *145*(2), 583-598, doi:10.1175/mwr-d-16-0034.1.
- 672 Lee, S.-H., Kim, E.-K., and Heo, I.-H. J. J. o. t. K. a. o. r. g. (2011a), A study on variability of extreme precipitation
673 by basin in South Korea, *17*(5), 505-520.
- 674 Lee, S.-W., Lee, D.-K., and Chang, D.-E. J. A. i. A. S. (2011b), Impact of horizontal resolution and cumulus
675 parameterization scheme on the simulation of heavy rainfall events over the Korean Peninsula, *28*(1), 1-15.
- 676 Lee, T.-Y., and Kim, Y.-H. (2007), Heavy Precipitation Systems over the Korean Peninsula and their Classification,
677 *Asia-Pacific Journal of the Atmospheric Sciences*, *43*, 367-396.
- 678 Lin, C., and Arakawa, A. J. J. o. t. a. s. (1997), The macroscopic entrainment processes of simulated cumulus
679 ensemble. Part I: Entrainment sources, *54*(8), 1027-1043.
- 680 Lin, Y., Zhao, M., Ming, Y., Golaz, J.-C., Donner, L. J., Klein, S. A., Ramaswamy, V., and Xie, S. (2013),
681 Precipitation Partitioning, Tropical Clouds, and Intraseasonal Variability in GFDL AM2 %J Journal of Climate,
682 *26*(15), 5453-5466, doi:10.1175/jcli-d-12-00442.1.
- 683 Lowrey, M. R. K., and Yang, Z.-L. (2008), Assessing the capability of a regional-scale weather model to simulate
684 extreme precipitation patterns and flooding in central Texas, %J Weather
685 *Forecasting*, *23*(6), 1102-1126.
- 686 Mishra, S. K., and Srinivasan, J. (2010), Sensitivity of the simulated precipitation to changes in convective
687 relaxation time scale, paper presented at Annales Geophysicae, Copernicus GmbH.
- 688 Mlawer, E. J., Taubman, S. J., Brown, P. D., Iacono, M. J., and Clough, S. A. (1997), Radiative transfer for
689 inhomogeneous atmospheres: RRTM, a validated correlated-k model for the longwave, *102*(D14), 16663-16682,
690 doi:<https://doi.org/10.1029/97JD00237>.
- 691 MOIS (2019), Ministry of Interior and Safety (MOIS). <https://www.mois.go.kr/frt/a01/frtMain.do>.
- 692 Molinari, J., and Dudek, M. J. M. W. R. (1992), Parameterization of convective precipitation in mesoscale
693 numerical models: A critical review, *120*(2), 326-344.
- 694 Mun, T., Park, C., Kim, G., and Cha, D.-H. (2019), Long-term Variability of Summer Heavy Rainfall in the Seoul
695 Metropolitan Area, *14*(4), 209-219.
- 696 Noh, Y., Cheon, W. G., Hong, S. Y., and Raasch, S. (2003), Improvement of the K-profile Model for the Planetary
697 Boundary Layer based on Large Eddy Simulation Data, *Boundary-Layer Meteorology*, *107*(2), 401-427,
698 doi:10.1023/A:1022146015946.
- 699 Olson, D. A., Junker, N. W., and Korty, B. (1995), Evaluation of 33 Years of Quantitative Precipitation Forecasting
700 at the NMC %J Weather and Forecasting, *10*(3), 498-511, doi:10.1175/1520-
701 0434(1995)010<0498:Eoyopp>2.0.Co;2.
- 702 Park, C.-Y., Moon, J.-Y., Cha, E.-J., Yun, W.-T., and Choi, Y.-E. J. J. o. t. K. G. S. (2008), Recent changes in
703 summer precipitation characteristics over South Korea, *43*(3), 324-336.
- 704 Prein, A. F., Langhans, W., Fossier, G., Ferrone, A., Ban, N., Goergen, K., Keller, M., Tölle, M., Gutjahr, O., and
705 Feser, F. J. R. o. g. (2015), A review on regional convection-permitting climate modeling: Demonstrations,
706 prospects, and challenges, *53*(2), 323-361.
- 707 Saito, K., Fujita, T., Yamada, Y., Ishida, J.-i., Kumagai, Y., Aranami, K., Ohmori, S., Nagasawa, R., Kumagai, S.,
708 and Muroi, C. J. M. W. R. (2006), The operational JMA nonhydrostatic mesoscale model, *134*(4), 1266-1298.

- 709 Shin, C.-S., and Lee, T.-Y. *J. J. o. t. M. S. o. J. S. I.* (2005), Development mechanisms for the heavy rainfalls of 6-7
710 August 2002 over the middle of the Korean Peninsula, *83*(5), 683-709.
- 711 Sims, A. P., Alapaty, K., and Raman, S. J. M. w. r. (2017), Sensitivities of summertime mesoscale circulations in the
712 coastal Carolinas to modifications of the Kain–Fritsch cumulus parameterization, *145*(11), 4381-4399.
- 713 Sun, J., and Lee, T.-Y. *J. J. o. t. M. S. o. J. S. I.* (2002), A numerical study of an intense quasi-stationary convection
714 band over the Korean Peninsula, *80*(5), 1221-1245.
- 715 Tokioka, T., Yamazaki, K., Kitoh, A., and Ose, T. *J. J. o. t. M. S. o. J. S. I.* (1988), The equatorial 30-60 day
716 oscillation and the Arakawa-Schubert penetrative cumulus parameterization, *66*(6), 883-901.
- 717 Wang, H., Zhang, M., and Liu, M. *J. o. A. M. S.* (2006), Influence of Moist Schemes in MM5 on the Uncertainties
718 of “03·7” Heavy Rainfall Numerical simulation, *17*(3), 346-353.
- 719 Wang, S., Sobel, A. H., Zhang, F., Sun, Y. Q., Yue, Y., and Zhou, L. *J. o. C.* (2015), Regional simulation of the
720 October and November MJO events observed during the CINDY/DYNAMO field campaign at gray zone resolution,
721 *28*(6), 2097-2119.
- 722 Wang, W., and Seaman, N. L. (1997), A Comparison Study of Convective Parameterization Schemes in a Mesoscale
723 Model *J Monthly Weather Review*, *125*(2), 252-278, doi:10.1175/1520-0493(1997)125<0252:Acsocp>2.0.Co;2.
- 724 Weisman, M. L., Skamarock, W. C., and Klemp, J. B. *J. M. W. R.* (1997), The resolution dependence of explicitly
725 modeled convective systems, *125*(4), 527-548.
- 726 Yang, M.-J., Chien, F.-C., Cheng, M.-D. *J. T., Atmospheric, and Sciences, O.* (2000), Precipitation Parameterization
727 in a Simulated Mei-Yu Front, *11*(2), 393-422.
- 728 Yu, X., Lee, T.-Y. *J. T. A. D. M., and Oceanography* (2010), Role of convective parameterization in simulations of
729 a convection band at grey-zone resolutions, *62*(5), 617-632.
- 730 Zheng, Y., Alapaty, K., Herwehe, J. A., Del Genio, A. D., and Niyogi, D. *J. M. W. R.* (2016), Improving high-
731 resolution weather forecasts using the Weather Research and Forecasting (WRF) Model with an updated Kain–
732 Fritsch scheme, *144*(3), 833-860.

1 **Impact of a scale-aware convective parameterization scheme on the simulation of**
2 **convective cells related heavy rainfall in South Korea**
3

4 **Haerin Park¹, Gayoung Kim¹, Dong-Hyun Cha¹, Eun-Chul Chang², Joowan Kim², Sang-**
5 **Hun Park³, Dong-Kyou Lee⁴**

6 ¹ Department of Urban & Environmental Engineering, Ulsan National Institute of Science and
7 Technology, Ulsan, South Korea

8 ² Department of Atmospheric Sciences, Kongju National University, Kongju, South Korea

9 ³ Department of Atmospheric Sciences, Yonsei University, Seoul, South Korea

10 ⁴ School of Earth and Environmental Sciences, Seoul National University, Seoul, South Korea

11
12 Corresponding author: Dong-Hyun Cha (dhcha@unist.ac.kr)

13 †School of Urban and Environmental Engineering

14 Ulsan National Institute of Science & Technology (UNIST)

15 50 UNIST-gil, Ulsu-gun, Ulsan 689-798, South Korea

16 Office) +82-52-217-2828, Fax) +82-52-217-2809

17
18
19 **Key Points:**

- 20 • We investigated the impact of the scale-aware convective parameterization scheme across
21 the gray-zone using the WRF model.
22
23 • The scale-aware CPS improved simulated convective cells related to rainfall by properly
24 removing atmospheric instability in the gray-zone.
25
26 • CAPE timescale and entrainment rate modulated in the scale-aware MSKF are the key
27 parameters for the improved rainfall simulation in the gray-zone.

28 Abstract

29 This study investigates the impact of the scale-aware convective parameterization scheme (CPS)
30 on convective cells related to simulation of heavy precipitation across the gray-zone using the
31 Weather Research and Forecasting (WRF) model. We select the Kain-Fritsch (KF) and Multi-
32 scale Kain-Fritsch (MSKF) schemes as non-scale-aware and scale-aware CPSs, respectively. The
33 MSKF scheme uses a scale-aware parameter that modulates the convective available potential
34 energy (CAPE) timescale and entrainment process in the KF scheme as a function of the
35 horizontal grid spacing. This study shows that simulation of convection only with grid-scale
36 process microphysics parameterization scheme (MPS) (i.e., explicitly resolved) causes an
37 unreasonably overestimated and erroneous location of precipitation in the gray-zone because
38 convection and atmospheric instability could not properly be triggered and reduced. Contrarily,
39 the CPS without scale-awareness in the gray-zone exaggerates the convection and distorts
40 synoptic fields, leading to the erroneous simulation of heavy precipitation at high resolution.
41 Contrastingly, the MSKF scheme with scale-awareness improves simulated convective cells
42 related to heavy rainfall by removing atmospheric instability in the gray-zone, smoothly reducing
43 the role of CPS and increasing the role of MPS as grid spacing is decreased. Additionally, the
44 sensitivity experiments show that the shorter CAPE timescale and decreased entrainment process
45 resulted in fast development and exaggeration of convective activities, respectively. These
46 parameters modulated by the scale-aware MSKF scheme can play a crucial role in the balanced
47 effect between the CPS and MPS in the gray-zone by controlling the entrainment rate and CAPE
48 timescale.

49 Plain Language Summary

50 With the increasing computer resources, Numerical weather prediction (NWP) models are
51 operating in the "gray zone" at horizontal grid spacing in the range of 1-10 km, where both
52 cumulus parameterization and explicit resolve are problematic. This study investigates the
53 impact of the scale-aware convective parameterization scheme (CPS) on convective cells in the
54 simulation of heavy precipitation across the gray-zone using the Weather Research and
55 Forecasting (WRF) model. The scale-aware CPS uses a scale-aware parameter that modulates
56 the convective process as a function of the horizontal grid spacing. We found that simulating
57 convection processes in the gray-zone without CPS is still limited because atmospheric
58 instability inadequately triggers or reduces it. Moreover, the CPS without scale-awareness
59 caused the erroneous precipitation simulation due to the exaggeration of convection and
60 distortion of the synoptic fields. Contrastingly, the scale-aware CPS improved the simulated
61 convection cells associated with heavy rainfall in the gray-zone by reducing the role of CPS and
62 increasing the role of explicitly resolved precipitation as grid spacing is decreased. Results
63 indicated that including scale-aware parameter in scale-awareness CPS plays a crucial role in
64 controlling the CPS and MPS in the gray-zone by controlling the convective processes.

65 **1 Introduction**

66 The precipitation characteristics in Korea have altered due to a changing climate. *Ha et*
67 *al.* (2005) and *Kwon et al.* (2007) showed that the East Asian summer monsoon changed since
68 the early mid-1990s. Several studies have shown that annual rainfall in Korea has tended to
69 increase. Notably, the frequency and intensity of precipitation increased considerably since the
70 1990s (*Kim et al.*, 2008; *Choi et al.*, 2013; *Mun et al.*, 2019). *Choi et al.* (2008) showed that
71 precipitation, especially in July and August, increased significantly. *Lee et al.* (2011a) indicated
72 that the annual precipitation amount from 2001 to 2010 considerably increased in July compared

73 to the past 30 years from 1970 to 2000. *Ho et al.* (2003) showed that the precipitation intensity in
74 early August was significantly enhanced due to the spatial difference in mid-level geopotential
75 height over the whole of Asia as a result of global warming. More than half of the annual
76 precipitation in Korea is concentrated in the summer (*Ho&Kang*, 1988; *Park et al.*, 2008), and
77 heavy rainfall during the summer monsoon is one of the robust characteristics of precipitation in
78 Korea, which causes considerable socioeconomic damage (*Kang et al.*, 1992). Various
79 precipitation systems generate heavy rainfall over the Korean Peninsula (e.g., band-type and
80 cluster) (*Sun&Lee*, 2002; *Shin&Lee*, 2005; *Cho&Lee*, 2006). Mesoscale convective systems
81 (MCSs) are the major types of heavy rainfall systems, which act over the Korean Peninsula
82 during the summer monsoon. Approximately 47% of heavy rainfall events between 2000 and
83 2006 were associated with MCSs (*Lee&Kim*, 2007). According to the Korean Ministry of the
84 Interior and Safety, the average annual number of death and the total property damages due to
85 heavy precipitation from 2009 to 2018 are 11.5 people and \$125 million, respectively (*MOIS*,
86 2019). More reliable and accurate predictions and a better understanding of the formation and
87 development mechanisms using observation data and numerical models are necessary to reduce
88 damage caused by heavy precipitation in Korea.

89 Many studies utilized a coarser horizontal grid spacing of the numerical models than the
90 actual horizontal scale of cumulus convection due to the limitation of computing resources. At
91 coarser resolutions with grid spacing larger than 10 km, the convective parameterization scheme
92 (CPS) is turned on to represent the effect of subgrid-scale convection on large-scale fields by
93 calculating the potential subgrid-scale cloud and physics of precipitation processes in association
94 with grid-scale independent and dependent variables. With the CPS, subgrid-scale convection is
95 possible even if the air parcel at the grid point is not saturated. Therefore, the CPS reduces delay

96 in precipitation or local instability, and it can represent the interaction between clouds and the
97 surrounding environment (*Bechtold et al.*, 2014; *Freitas et al.*, 2018; *Han et al.*, 2011). Many
98 studies (*Wang&Seaman*, 1997; *Yang et al.*, 2000) have shown that numerical simulation can be
99 sensitive to the chosen parameterization schemes compared to those of the other factors (e.g.,
100 domain setup and studied cases). *Jankov et al.* (2007) and *Lowrey and Yang* (2008) indicated that
101 the different parameterization schemes (e.g., CPS and microphysics parameterization scheme
102 (MPS)) resulted in different simulation results, and especially the CPS showed a significant
103 impact on precipitation simulation. Parameterized convection at coarse horizontal grid spacing
104 has limitations and causes inaccurate precipitation simulations (e.g., *Emanuel&Raymond*, 1993;
105 *Olson et al.*, 1995; *Wang&Seaman*, 1997). Therefore, efforts to improve the CPS are required to
106 reduce the prediction error of the convection process in the subgrid-scale (*Wang et al.*, 2006;
107 *Dudhia*, 2005).

108 According to tremendous numerical computing and atmospheric modeling technology
109 that can support high-resolution modeling, the grid sizes of numerical weather models are now
110 close to 2–10 km (*Davies et al.*, 2005; *Saito et al.*, 2006; *Charles et al.*, 2009). Although a higher
111 resolution allows for more accurate representations of surface fields and topography, it is
112 generally difficult to define the range of convection process between the subgrid-scale to be
113 parameterized using CPS and the grid-scale to be explicitly resolved (*Hong&Dudhia*, 2012;
114 *Molinari&Dudek*, 1992; *Jeworrek et al.*, 2019), which is called “gray-zone (1–10 km)”
115 (*Gerard&oceanography*, 2007). The development of CPS for the gray-zone in the numerical
116 model remains a problem (*Hong&Dudhia*, 2012).

117 Generally, the CPS is not required as explicitly resolved convections are considered
118 sufficient in grid intervals under the gray-zone. *Wang et al.* (2015) shows that the regional

119 models with 9-km grid spacing can capture the salient characteristics of precipitation over the
120 tropics without CPS. In *Molinari and Dudek (1992)* and *Weisman et al. (1997)*, the horizontal
121 grid spacing is 4 km or less, and it can explicitly consider convection-permitting without relying
122 on CPS at this resolution. *Yu et al. (2010)* indicate that a grid size of 3 km is sufficient to resolve
123 the convection band and CPS for this grid size is not necessary.

124 Contrarily, studies have shown that high-resolution numerical models only with MPS
125 (i.e., no CPS) still have limitations in simulating convection processes (*Arakawa et al., 2016*;
126 *Gustafson et al., 2013*). *Deng et al. (2006)* showed that the simulated precipitation skill of a 4-
127 km grid improved when CPS was used. Furthermore, *Lee et al. (2011b)* showed that the
128 numerical model improves heavy rainfall forecast by activating both the CPS and MPS at fine
129 grid size (e.g., 3 km). There are still ambiguous results for the CPS activation at grid spacings
130 smaller than 3 and 4 km. Consequentially, there remains an effort to adjust or improve the CPS
131 validity in the gray-zone (*Arakawa et al., 2011*; *Hong&Dudhia, 2012*; *Prein et al., 2015*;
132 *Bengtsson&Körnich, 2016*; *Zheng et al., 2016*). Such new schemes are designed to be scale-
133 aware, such that they can represent smooth transition grid intervals. *Sims et al. (2017)* showed
134 that an applied scale-aware parameter, which is a function of horizontal resolution, determined
135 the simulation performance of mesoscale convection phenomena, and the Kain-Fritsch scheme
136 (KF) modified by the scale-aware parameter could improve the convection timing of the
137 mesoscale convection phenomenon in the Carolinas region. *Kwon and Hong (2017)* applied the
138 scale-aware parameters in the Simplified Arakawa-Schubert scheme at 3 km, which improved
139 simulated precipitation over the Korean Peninsula by the summer monsoon. A study by *Jeworrek*
140 *et al. (2019)* consisted of five domains with different horizontal model resolutions (27, 9, 3, 1,
141 and 0.3 km) to investigate the predictability of the CPSs with scale-aware parameters in the gray-

142 zone. Their study testing the effect of scale-aware CPS showed significant improvement in the
143 location, pattern, and intensity of precipitation at high resolution. The role of CPS is gradually
144 reduced to reproduce the smooth reduction from subgrid-scale to grid-scale precipitation with
145 increasing resolution.

146 Summarily, the physics of the sub-grid precipitation process plays an essential role in the
147 simulation of precipitation over the Korean Peninsula, and studies showed that the importance of
148 smooth CPS activation using scale-aware parameters increased with higher resolution (*Alapaty et*
149 *al.*, 2012; *Sims et al.*, 2017; *Kwon&Hong*, 2017; *Jeworrek et al.*, 2019). Thus far, various
150 numerical studies have been conducted to understand the effect of high-resolution models in
151 simulating heavy rainfall events over the Korean Peninsula (*Hong&Lee*, 2009; *Kwon&Hong*,
152 2017). However, studies on the role of scale-aware parameterization schemes in the gray-zone
153 are still limited for heavy rainfall cases in the Korean Peninsula. Therefore, this study
154 investigated the effect of scale-aware parameters on a gray-zone domain using non-scale-aware
155 and scale-aware CPS for a heavy rainfall case in Korea. In this study, the KF (*Kain*, 2004) and
156 the Multi-scale Kain-Fritsch (MSKF) schemes (*Zheng et al.*, 2016) are selected for CPSs. The
157 MSKF scheme is a scale-aware version of the KF scheme, in which the CAPE timescale and
158 entrainment rate are adjusted according to the horizontal grid spacing. A flash flooding event in
159 the central region of the Korean Peninsula from 15 to 17 July 2017, is selected as the heavy
160 rainfall case. The case is spatially and temporally localized and is suitable for analyzing
161 precipitation sensitivity to the applied non-scale and scale-aware CPS in the gray-zone.

162 Simulations of numerical models are influenced by various CPS factors, such as the
163 CAPE timescale and entrainment rate. In the model, the CAPE timescale plays a role in the
164 dissipation of the deep moist convection instability during that period and determines the cloud

165 lifetime (*Mishra&Srinivasan*, 2010). Additionally, the entrainment rate changes the convective
166 process by determining the saturation and mixing with the surrounding dry air (*Lin&Arakawa*,
167 1997; *Kuang&Bretherton*, 2006; *Khairoutdinov&Randall*, 2006). Therefore, we conducted
168 sensitivity experiments to examine the impacts of the scale-aware parameter on the CAPE
169 timescale and entrainment rate in the MSKF scheme.

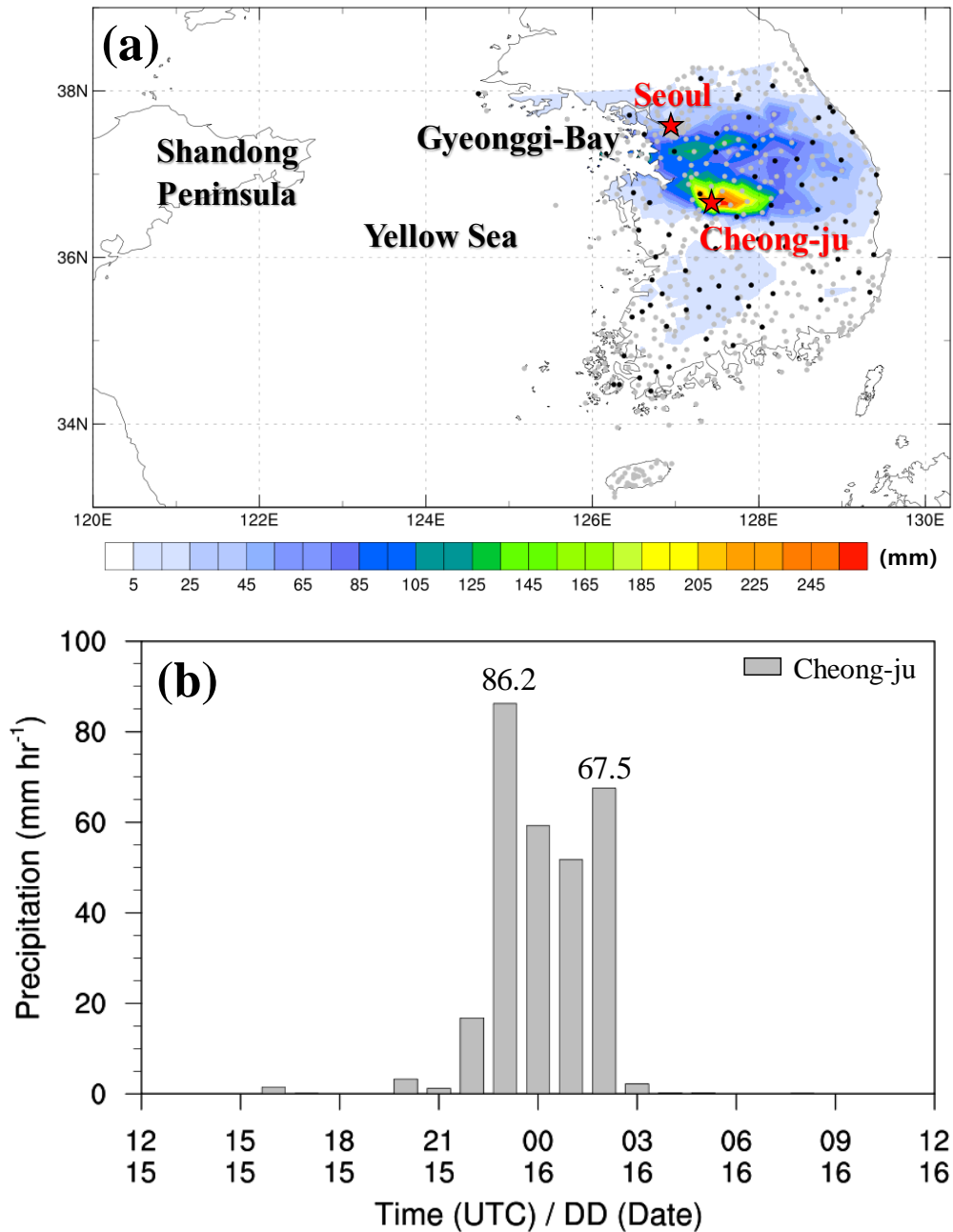
170 The rest of the paper is organized as follows. Section 2 describes the studied heavy
171 rainfall case and numerical experimental design. Section 3 shows the results from the numerical
172 experiments with different CPSs and sensitivities to the scale-aware parameter. Finally, the
173 summary and conclusions are provided in Section 4.

174 **2 Case and Experimental Design**

175 2.1 Characteristics of Cheong-ju rainfall case

176 A significant amount of extreme precipitation was recorded in Cheong-ju city on 16 July
177 2017 (Figure 1a), with a maximum daily rainfall of 290.2 mm. In Choeng-ju (marked as a red
178 star in Figure 1a), the rainfall started at 2000 UTC, 15 July (0500 LST, 16 July), and the first and
179 second peaks occurred at 2300 UTC, 15 July and 0200 UTC, 16 July, respectively (Figure 1b).
180 Hourly rainfall rates peaked at 2300 UTC with 86.2 mm hr⁻¹ and 0200 UTC with 67.5 mm hr⁻¹.
181 Subsequently, the rainfall almost stopped at 0300 UTC on 16 July 2017.

182



183

184 **Figure 1.** (a) Map of the study area showing the 24-hour accumulated rainfall amounts (mm)
 185 observed by automated surface observation systems (ASOS, black dots) and automatic weather
 186 stations (AWS, gray dots) in the central Korean Peninsula from 1200 UTC (2100 LST), 15 to
 187 1200 UTC (2100 LST), 16 July 2017 (The star mark denotes the location of Seoul and Cheong-
 188 ju), and (b) Bar plot of the time series of hourly rainfall from Cheong-ju, from
 189 1200 UTC (2100 LST), 15 to 1200 UTC (2100 LST), 16 July 2017.

190

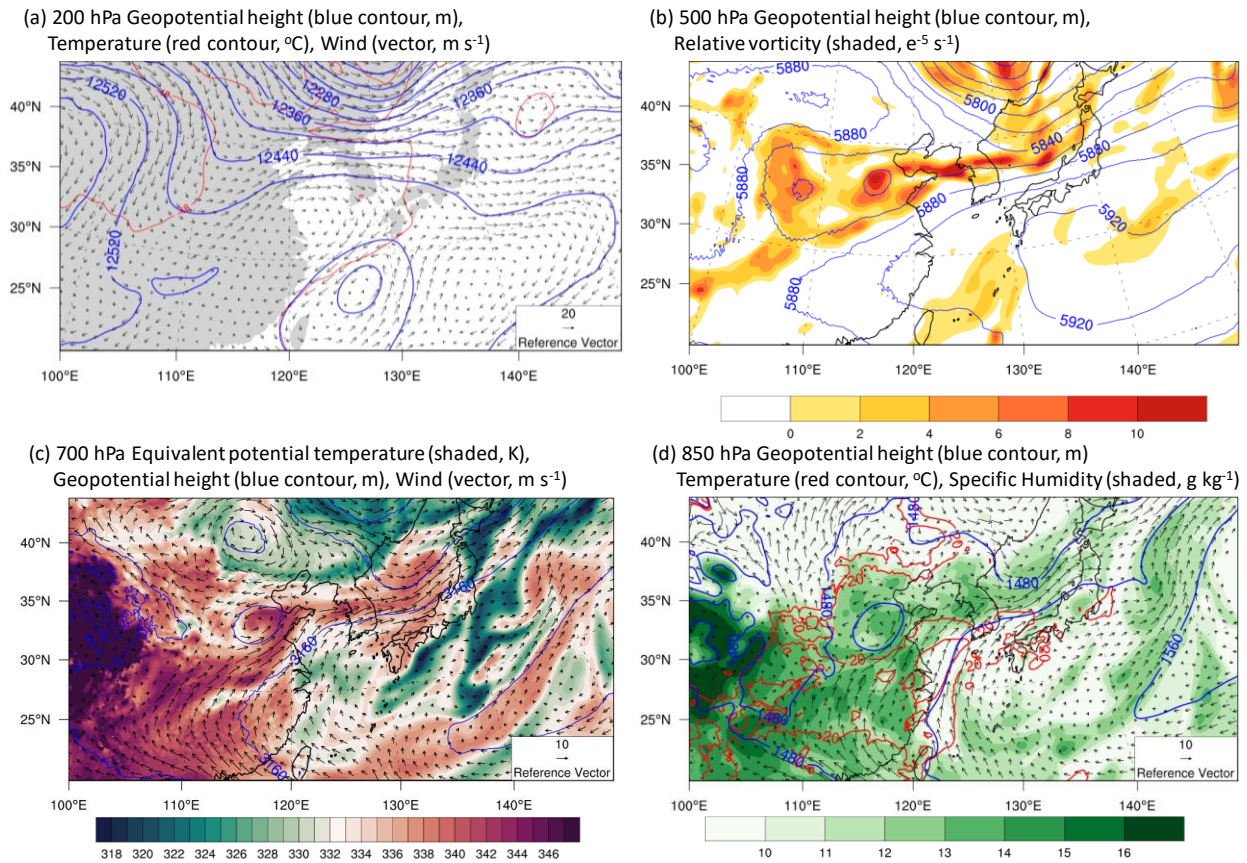
191

192 Figure 2 shows the synoptic fields of four pressure levels analyzed by the FNL 0.25°
193 reanalysis data at 1800 UTC, 15 July 2017, which was 6 h before the maximum precipitation
194 intensity in Cheong-ju. At 200 hPa (Figure 2a), an upper-pressure trough developed west of the
195 Shandong Peninsula and a shallow upper-pressure ridge in the south of the Shandong Peninsula
196 extending to South Korea. Figure 2b and d show that the western North Pacific subtropical high
197 (WNPSH) is expanded to the Korean Peninsula, forming a confluent flow region, and warm and
198 humid water vapor is transported into the central region in the Korean Peninsula. Notably,
199 positive relative vorticity is dominant over the central region of the Korean Peninsula, where the
200 southwesterly enhances continuous moisture transportation (Figure 2b). Additionally, the
201 divergence areas are consistent with the water vapor convergent flow areas at the lower level
202 (i.e., the Shandong Peninsula and the Korean Peninsula), indicating that both dynamic and
203 thermodynamic environments induced rising motion at the mid-level (see supplementary Figure
204 S1). Due to the unstable conditions, the quasi-stationary front (Changma front) is initiated from
205 the west of the Shandong Peninsula (along the isotherm of 333 K in Figure 2c), where a robust
206 upper-level trough expands to the Korean Peninsula. Environmental conditions such as upper-
207 level divergence, abundant water vapor supply, and significant atmospheric instability are
208 favorable for developing a convection system. *Chung et al. (2019)* found that warming in the
209 northern part of the Changma front resulted in less meridional temperature contrast and an
210 unstable atmosphere repeating a small disturbance that has moved along the boundary in the
211 WNPSH, which resulted in discontinuous cloud bands and intermittent rainfall. A discontinuous
212 broken Changma front with strong convective cells is represented through the 3-hourly enhanced
213 IR satellite images from 1600 UTC, 15 July to 0100 UTC, 16 July (Figure 3). In the enhanced IR
214 images, there are two convective cells: a convective cell (hereafter referred to as CC1) that has

215 begun to develop off the coast of Gyeonggi-bay and a deep-developed convective cell (hereafter
 216 called CC2) in the south of Shandong Peninsula. Eventually, the CC1 generated on Gyeonggi-
 217 bay gradually developed and advanced to the southeast (Figure 3a and b). All precipitation of
 218 this investigated event was associated with CC1. Another convective cell (i.e., CC2) developed
 219 in the south of the Shandong Peninsula, which moved into the Yellow Sea over time. These
 220 cloud systems result from the rising motion and substantial low-level convergent area from the
 221 activated quasi-stationary front accompanied by heavy rainfall.

222

223

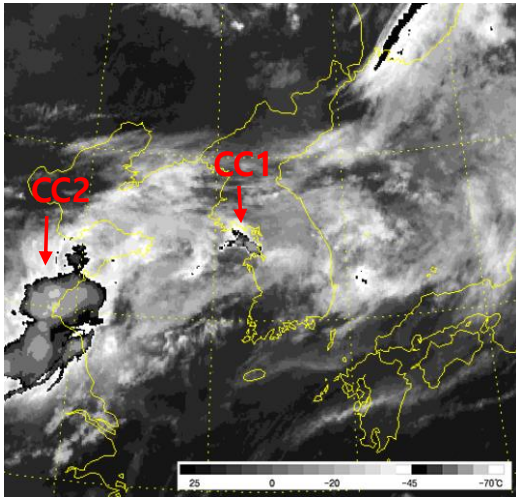


224

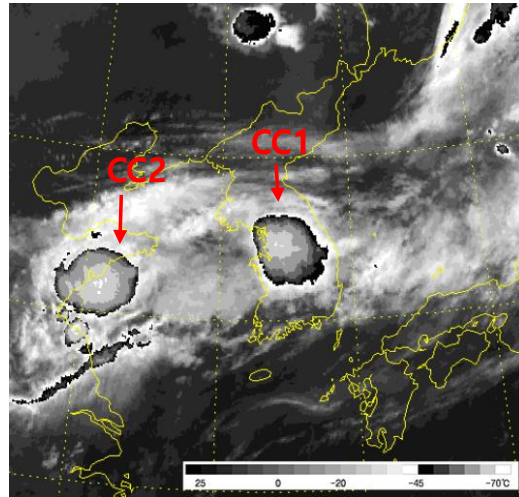
225 **Figure 2.** Spatial contour maps showing the synoptic fields from FNL 0.25° reanalysis data at
 226 1800 UTC, 15 July 2017.

227

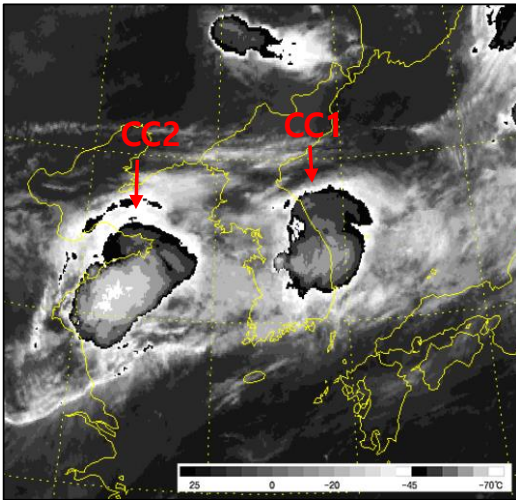
(a) 1600 UTC July 15



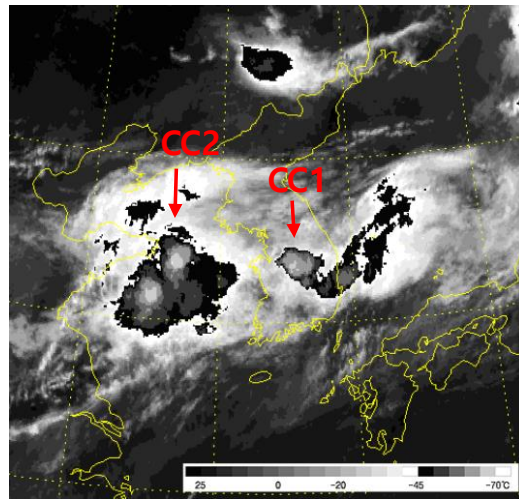
(b) 1900 UTC July 15



(c) 2200 UTC July 15



(d) 0100 UTC July 16



228
229

230 **Figure 3.** Three-hourly Enhanced IR satellite images showing cloud system development between
231 1600 UTC, 15 July and 0100 UTC, 16 July 2017.

232
233

234 2.2 Model configuration and experiment design

235

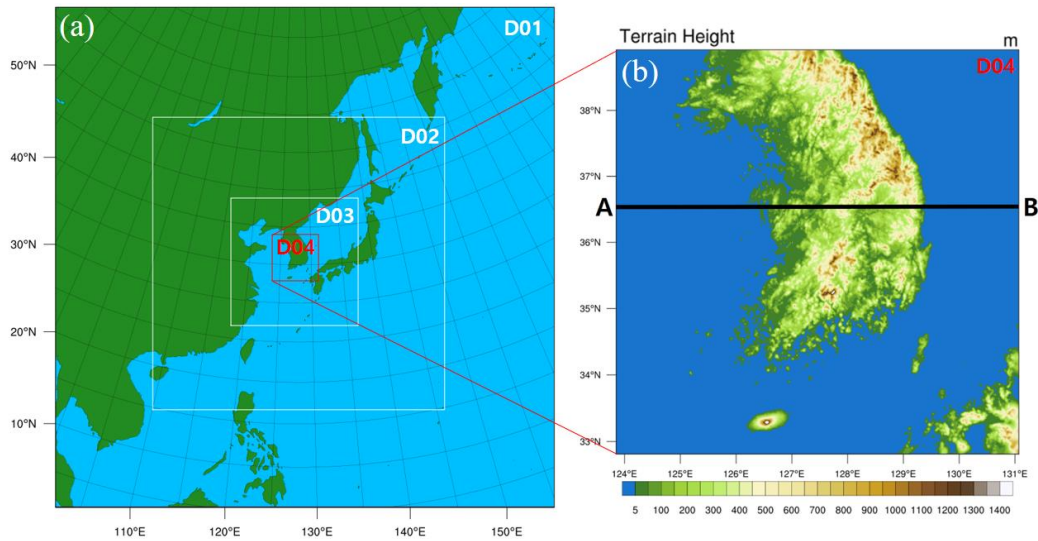
236 The Advanced Research WRF model (Skamarock et al., 2008) Version 4.1 was used in

237 this study, and the initial and boundary conditions were obtained from the $1^\circ \times 1^\circ$ reanalysis data

238 of the National Centers for Environmental Prediction/National Centers for Atmospheric
239 Research (NCEP/NCAR) Final analysis (FNL). The model consisted of four domains with 36 km
240 (201×201), 12 km (352×352), 4 km (460×460), and 1.33 km (201×201) horizontal grid spacings,
241 which included CPS gray-zone resolution (Figure 4a). We used two-way nested domains with a
242 Lambert conformal map projection. The domain contained 32 vertical levels from the surface to
243 the top of the atmosphere at 50 hPa. The model used the WSM6 cloud microphysics scheme
244 (*Hong&Lim, 2006*), the Yonsei University planetary boundary layer scheme (*Noh et al., 2003*;
245 *Hong et al., 2006*), Dudhia short-wave radiation scheme (*Dudhia, 1989*), and long-wave
246 radiation scheme based on the rapid radiative transfer model (*Mlawer et al., 1997*). In this study,
247 the KF scheme and MSKF schemes were selected for the sensitivity experiments. The KF
248 scheme is a sub-grid scheme with deep and shallow convection and uses a mass flux approach to
249 calculate the CAPE-based closure assumption scheme. The MSKF scheme is a scale-aware
250 version of the KF scheme. Compared to the KF, the MSKF includes changes in the convective
251 adjustment timescale and improvements to the entrainment formulations (*Zheng et al., 2016*).
252 The MSKF also incorporates a grid-aware scaling parameter into these modifications. The main
253 advantages of the MSKF scheme are as follows.

254

255



256

257 **Figure 4.** Map showing (a) Four nested domains with 36 km, 12 km, 4 km, and 1.33 km grid
 258 spacing in WRF, and (b) terrain height for the finest domain (red box identified as the D04
 259 domain in Figure 4a). Line AB in Figure 4b marks the vertical cross-section used in Figure 10.

260

261 Both the KF and MSKF schemes remove 90% of the potential energy within the CAPE
 262 timescale period (*Bechtold et al.*, 2001), and the CAPE timescale is limited to 1800 s and 3600 s
 263 in the cloud layer for deep and shallow convections, respectively. The convection time step (τ)
 264 connected to the CAPE timescale of clouds is proportional to the grid length DX (*Fritsch et al.*,
 265 1976; *Fritsch&Chappell*, 1980). The CAPE timescale works to effectively resolve atmospheric
 266 instability at coarse grid resolution. However, the higher model grid resolution leads to an
 267 increase in the unresolved cloud area and faster saturation speed, which causes rapid CAPE
 268 removal problems within the CAPE timescale resulting in intense precipitation. For reduction of
 269 these inadequacies, the MSKF scheme uses the adjustment timescale τ (s) based on *Bechtold et*
 270 *al.* (2008), which is multiplied by the scaling parameter (β) impacted by the horizontal grid-scale
 271 (*Zheng et al.*, 2016).

272 The CAPE adjustment timescale can be estimated as:

$$273 \quad \tau = \frac{H}{(\delta m_b A_e)^{\frac{1}{3}}} \beta, \quad (1)$$

274 where H is cloud depth (m), δm_b is the updraft mass flux of cloud base per unit density
 275 (m s^{-1}), A_e is the potential energy of the saturated air supplied to the cloud base ($\text{m}^2 \text{s}^{-2}$), and β is
 276 the scaling parameter defined as

$$277 \quad \beta = 1 + \ln\left(\frac{25}{DX}\right). \quad (2)$$

278 β is set to approximately 2.8 and 4.2 at 4 and 1 km model grid spacings in equation (2),
 279 respectively. As the grid spacing decreases, the CAPE adjustment timescale using the scale-
 280 aware parameter becomes longer. A longer CAPE timescale allows slower elimination
 281 convective instability.

282 Additionally, the MSKF scheme adjusts the minimum entrainment rate using the scale-
 283 aware parameter similar to the timescale concept. The adjusted entrainment rate is defined as:

$$284 \quad \Delta M_e = M_b \frac{\alpha \beta}{Z_{LCL}} \Delta p, \quad (3)$$

285 where M_b is the updraft mass flux per unit area (kg s^{-1}) at the cloud base, β is the scale-
 286 aware parameter (eq. 2), Δp is the pressure depth of a model level (Pa), and Z_{LCL} (m) is the
 287 height of the cloud base. The value of α (0.03) is a constant parameter (*Tokioka et al.*, 1988). The
 288 cloud base height replaces the arbitrarily fixed cloud radius because entrainment is associated
 289 with the sub-cloud layer depth. The mixing rate increases with the β value, limiting the sub-grid
 290 convection (*Lin et al.*, 2013). This adjusted scale-aware entrainment formulation allows the
 291 mixing rate, ΔM_e , to increase with decreasing horizontal grid spacing. At higher resolutions, the
 292 effects of the KF scheme are reduced, which inhibits deep convection.

293 The experiments conducted in this study consist of two parts. In Part 1, three experiments
 294 were conducted to investigate the difference between the KF and MSKF schemes and the impact
 295 of CPS in the gray-zone (KF_D12, KF, and MSKF runs). The KF_D12 run employed the KF
 296 scheme only in D01 and D02 domains with 36 and 12 km resolutions, respectively, while the KF
 297 and MSKF runs used the KF and MSKF schemes in all domains, respectively. In Part 2, we
 298 conducted two additional experiments (CTS and ENT) to investigate the effects of the scale-
 299 aware parameter in the MSKF scheme on the convective activity simulation causing heavy
 300 rainfall. The CTS run is the same as the MSKF run but for the scale-aware parameter value of 1
 301 in the CAPE timescale (i.e., the same CAPE timescale as in the KF scheme), and the ENT run is
 302 identical to the MSKF scheme except for the same entrainment rate as in the KF scheme. As the
 303 horizontal model resolution increases (e.g., D03 or D04 domains), we can examine the effect of
 304 the scale-aware parameter on the reduced (increased) CAPE timescale (entrainment rate) of the
 305 MSKF scheme by comparing the CTS (ENT) and MSKF runs. The experiments conducted in
 306 this study are summarized in Table 1.

307 **Table 1. List of experiments conducted in this study.**

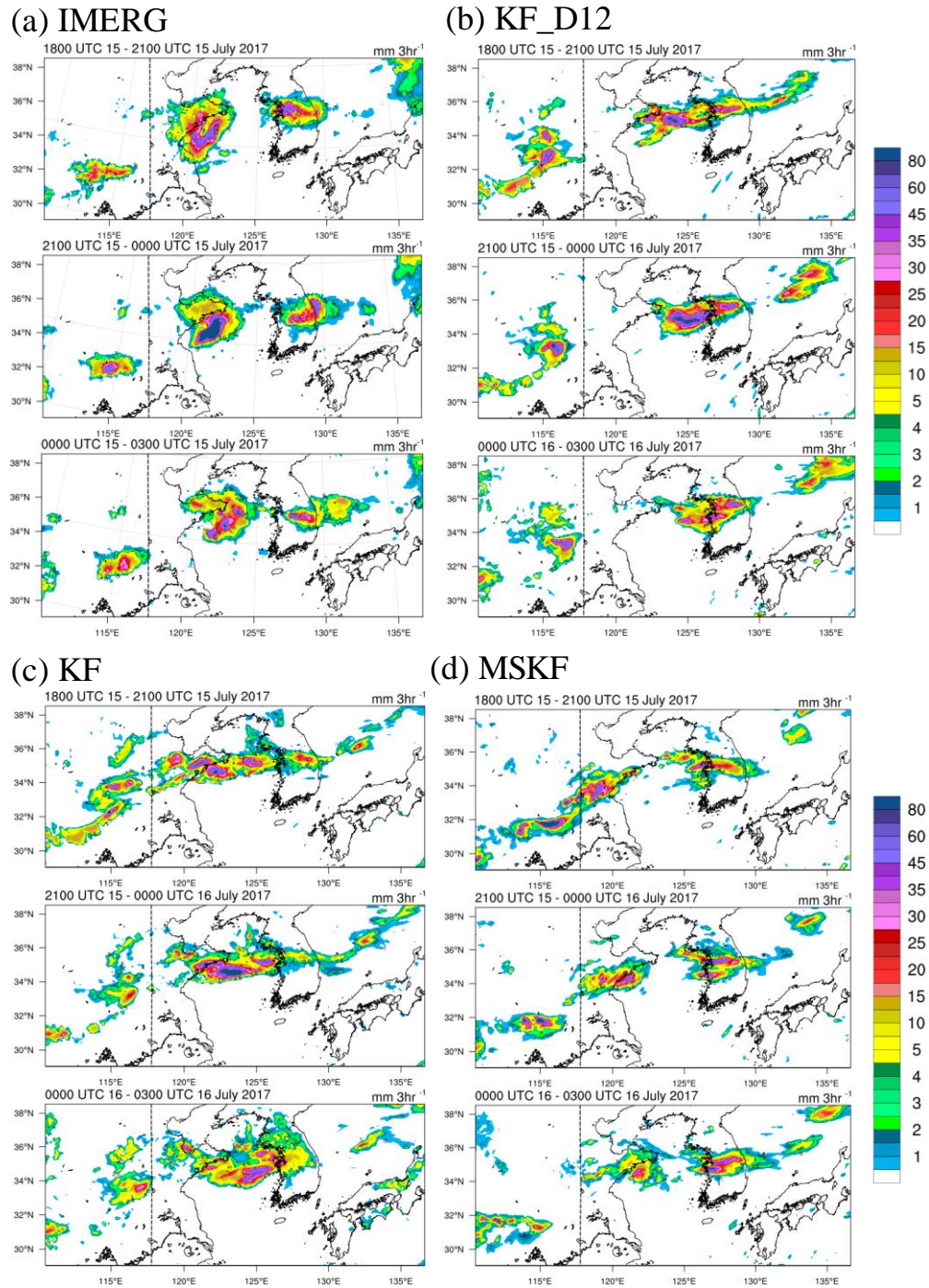
Experiments	Description
KF_D12	KF scheme used only for the D01 and D02 domains
KF	KF scheme used for all domains
MSKF	MSKF scheme used for all domains
CTS	Same as MSKF run, but for the same CAPE timescale as in KF scheme
ENT	Same as MSKF run, but for the same entrainment as in KF scheme

308

309 **3 Results**

310 3.1 Difference between the KF and MSKF schemes and CPS impact on the gray-zone

311 In this section, simulated precipitation from the KF_D12, KF, and MSKF runs was
312 compared with the Integrated Multi-SatellitE Retrievals for Global Precipitation Measurement
313 (IMERG, *Huffman et al.*, 2015a; 2015b) and FNL 0.25° reanalysis data to analyze the differences
314 in rainfall and synoptic fields among the three runs. As mentioned in Figure 3, two types of
315 precipitation zones were observed in Figure 5a. One was the precipitation zone caused by CC1,
316 which started over the Seoul metropolitan region (Gyeonggi-bay) and moved southeastward.
317 Another related to CC2 moved from the Shandong Peninsula to the Yellow Sea. The IMERG
318 satellite image indicates that the precipitation area related to CC1 over Gyeonggi-bay moved
319 southeastward, resulting in heavy rainfalls in Cheong-ju. Figure 5b-d shows the 3-hourly
320 accumulated total (subgrid-scale and grid-scale) precipitation in the D02 domain of three runs. In
321 the KF_D12 run (Figure 5b), CC1 was located over the eastern part of Seoul and was expanded
322 northeastward; the model simulated simply one convective system instead of two convective
323 systems. Furthermore, unreasonable shifting of the simulated precipitation associated with CC2
324 to the Yellow Sea instead of the southern part of the Shandong Peninsula caused an error of
325 overestimated rainfall in the ocean. The KF run (Figure 5c) simulated similar features to the
326 KF_D12 run (i.e., overestimated precipitation over the Gyeonggi-Bay). However, the
327 precipitation core was shifted west in KF run compared to the KF_D12 run. Contrastingly, the
328 MSKF run (Figure 5d) reproduced the spatial pattern of simulated precipitation more correctly
329 relative to KF_D12 and KF runs. Notably, in the MSKF run, CC1 and CC2 were simulated
330 separately, similar to those in the IMERG. Hence, the heavy rainfall related to CC1 was
331 reasonably captured.

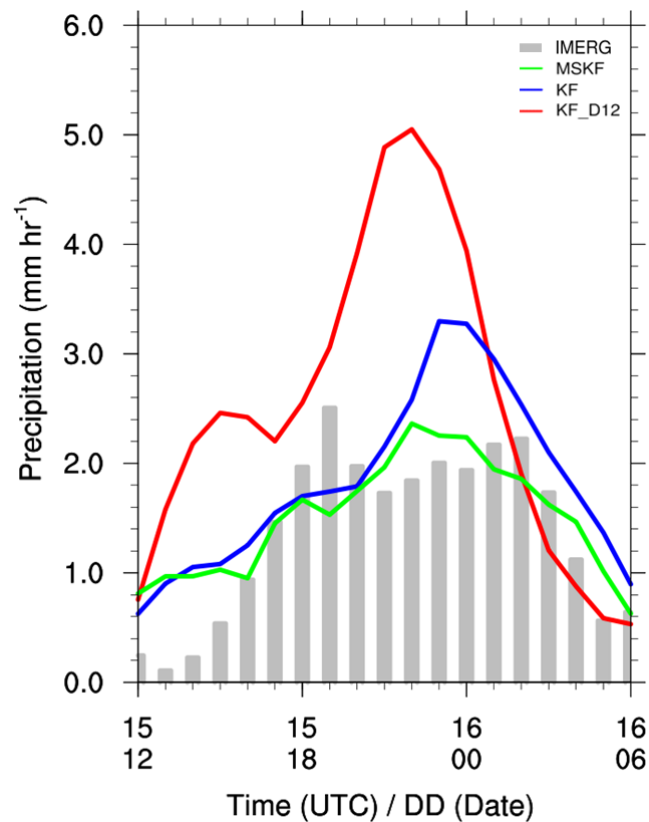


332

333 **Figure 5.** Spatiotemporal images showing three-hourly accumulated total precipitation (mm) in
 334 the D02 domain between 1800 UTC, 15 July and 0300 UTC, 16 July 2017. Black dashed lines
 335 indicate the left boundary of the D03 domain in Figure 3a.

336

337 Figure 6 shows the time series of domain-averaged hourly precipitation for observed
 338 (IMERG) and simulated precipitation (i.e., the D02 domain) averaged for the target region,
 339 including the Korean Peninsula and the Yellow Sea. Heavy precipitation was observed for 18
 340 hours (1200 UTC, 15 July to 0300 UTC, 16 July), with two peaks at 1800 UTC 15 and 0300
 341 UTC 16. However, the KF_D12 run reproduced the two heavy precipitation peaks earlier than in
 342 the observation with the overestimated precipitation due to unreasonable simulation in the
 343 Yellow Sea. The simulated precipitation of the KF run is more reasonable than the KF_D12 run.
 344 However, the precipitation in the target region was still overestimated than IMERG.
 345 Contrastingly, the MSKF run simulated heavy precipitation most reasonably in the target region
 346 in terms of amount.



347

348 **Figure 6.** Graph depicting time-series of hourly accumulated rainfall averaged between 36-
 349 38 °N and 123-130 °E for the IMERG (gray box), KF_D12 (red line), KF (blue line), and MSKF

350 (green line) run. Simulated precipitation is calculated from the results of the 4-km resolution
 351 domain.

352

353 To quantitatively evaluate the performance of the heavy precipitation simulation (Figure
 354 7), we calculated two standard skill scores (i.e., the treat score (TS) and bias score (BS)) for
 355 precipitation with various precipitation intensity thresholds (e.g., 0.5, 5, 10, 20, 30, 40, and 50
 356 mm). Two scores were calculated using the following equations (Eq. 4 and 5) (Wilks, 2011). As
 357 BS and TS approach 1, the accuracy of the model in forecasting rainfall events increases.

358

$$359 \quad BS = \frac{Hits + False\ alarms}{Hits + Misses}, \text{ and} \quad (4)$$

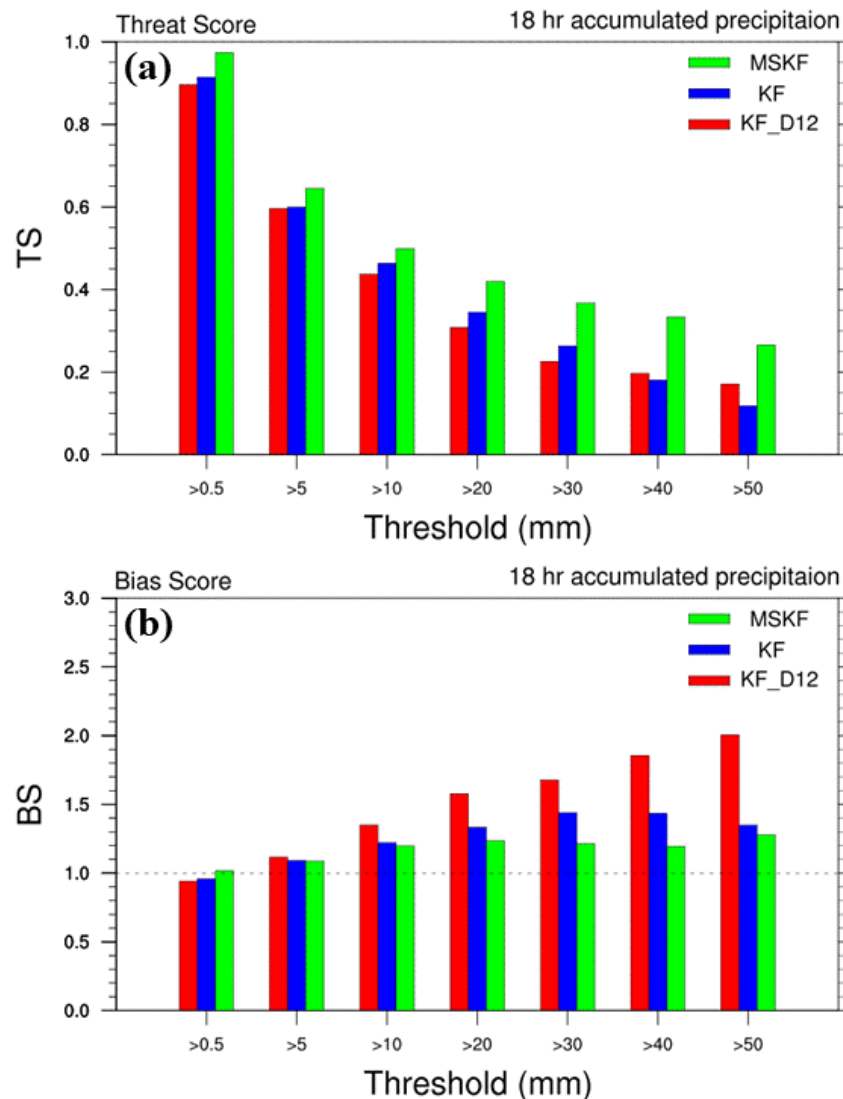
$$360 \quad TS = \frac{Hits}{Hits + False\ alarms + Misses}. \quad (5)$$

361

362 The precipitation detection skills (e.g., BS and TS) decreased as the threshold increased
 363 in the three runs (Figure 7). The TS for the precipitation forecast is the highest in the MSKF run
 364 compared to the other runs (e.g., the KF_D12 and KF runs) for all the considered precipitation
 365 thresholds. In the TS, the KF and KF_D12 runs have a low score than the MSKF run across the
 366 entire range of precipitation intensity thresholds. The result of the BS indicates that the KF and
 367 KF_D12 runs simulated more ‘false alarms’ and ‘misses’ than ‘hits’ compared to those of the
 368 MSKF run. In the BS, the MSKF run has high model performance in detecting precipitation
 369 across the entire range of precipitation intensities by maintaining the BS value of around 1.
 370 However, the BS in the KF and KF_D12 runs increases more significantly than in the MSKF
 371 run. Notably, the BS in the KF_D12 run increases dramatically as the threshold increases,
 372 suggesting that in the low performance of the KF_D12 run, the number of falsely classified grid

373 boxes as ‘false alarms’ tends to be substantially larger than the number of incorrectly classified
 374 grid boxes as ‘misses’. The KF_D12 run has many ‘false alarms’ due to excessive precipitation
 375 in the Yellow Sea before entering the Koran Peninsula. In the KF and KF_D12 runs, as a result,
 376 the overall forecasting abilities of the precipitation products in capturing the correct magnitude
 377 of intense precipitation are less accurate than that in the MSKF run.

378



379

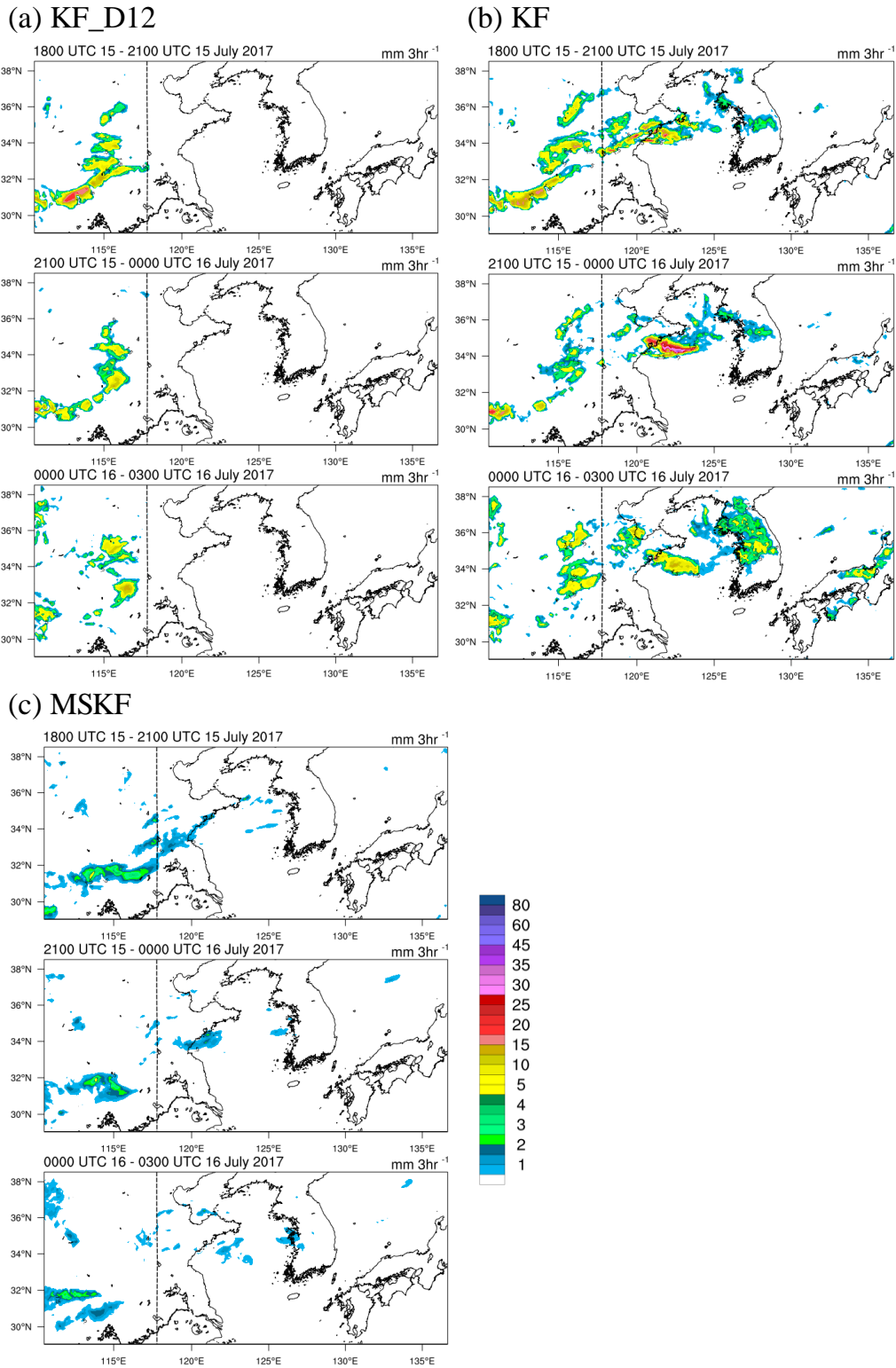
380

381 **Figure 7.** Bar plots of the statistical indices corresponding to the KF_D12, KF, and MSKF runs
 382 with IMERG based on different thresholds of 18-hourly accumulated precipitation (from 1200

383 UTC, 15 July to 0600 UTC, 16 July 2017). The simulated precipitation is interpolated to the
384 observation grid points, and model statistics are calculated for South Korea and the Yellow Sea
385 (between 36-38 °N and 123-130 °E).

386

387 Figure 8 shows the distribution of subgrid-scale precipitation simulated by the CPS. The
388 KF run simulated subgrid-scale precipitation is similar to the KF_D12 run in the D02 domain
389 outside the D03 domain. However, within the D03 domain, only the KF run simulated subgrid-
390 scale precipitation employing CPS for the domain. The KF_D12 run could not produce subgrid-
391 scale precipitation because of the absence of CPS in the D03 domain. Contrastingly, the subgrid-
392 scale precipitation simulated in both the D02 and D03 domains of the MSKF run was reduced
393 compared with that in the KF run. The MSKF scheme simulates a smaller ratio of subgrid-scale
394 precipitation to total precipitation than in the KF scheme as the horizontal resolution increases
395 because the scale-aware parameter in the MSKF scheme smoothly decreases the role of CPS and
396 increases the removal of atmospheric instability by MPS.



397

398 **Figure 8.** Spatiotemporal images (similar to Figure 5) for three-hourly accumulated subgrid-
 399 scale precipitation (mm).

400

401 To investigate the causes of the different simulations among the three runs, we analyzed
402 the synoptic conditions from the reanalysis and simulations of the D02 domain in Figure 9. In FNL
403 (Figure 9a), LLJ ($> 13 \text{ m s}^{-1}$) transporting wet and warm air was located in two regions (e.g., the
404 Shandong and Korean Peninsulas) with heavy precipitation. (see Figure 5a). The three WRF runs
405 reproduced wet and warm air transport by LLJ from inland China to the Korean Peninsula.
406 However, the LLJ cores were inappropriately located in inland China and the Yellow Sea in the
407 KF_D12 and KF runs (Figure 9b, c), and the intensity of LLJ was overestimated, which induced
408 enhanced moisture transport. Notably, LLJs located at the Shandong Peninsula in the reanalysis
409 were further shifted to the Yellow Sea in the KF_D12 run. Additionally, low-pressure systems at
410 700 hPa unrealistically developed in the LLJ cores in the KF_D12 and KF runs. More moisture
411 transported by the enhanced LLJ led to increased convective instability over the regions, which
412 developed convective activities and low-level pressure erroneously. Contrarily, the MSKF run
413 reproduced the low-pressure system and LLJ similar to the reanalysis regarding location and
414 intensity.

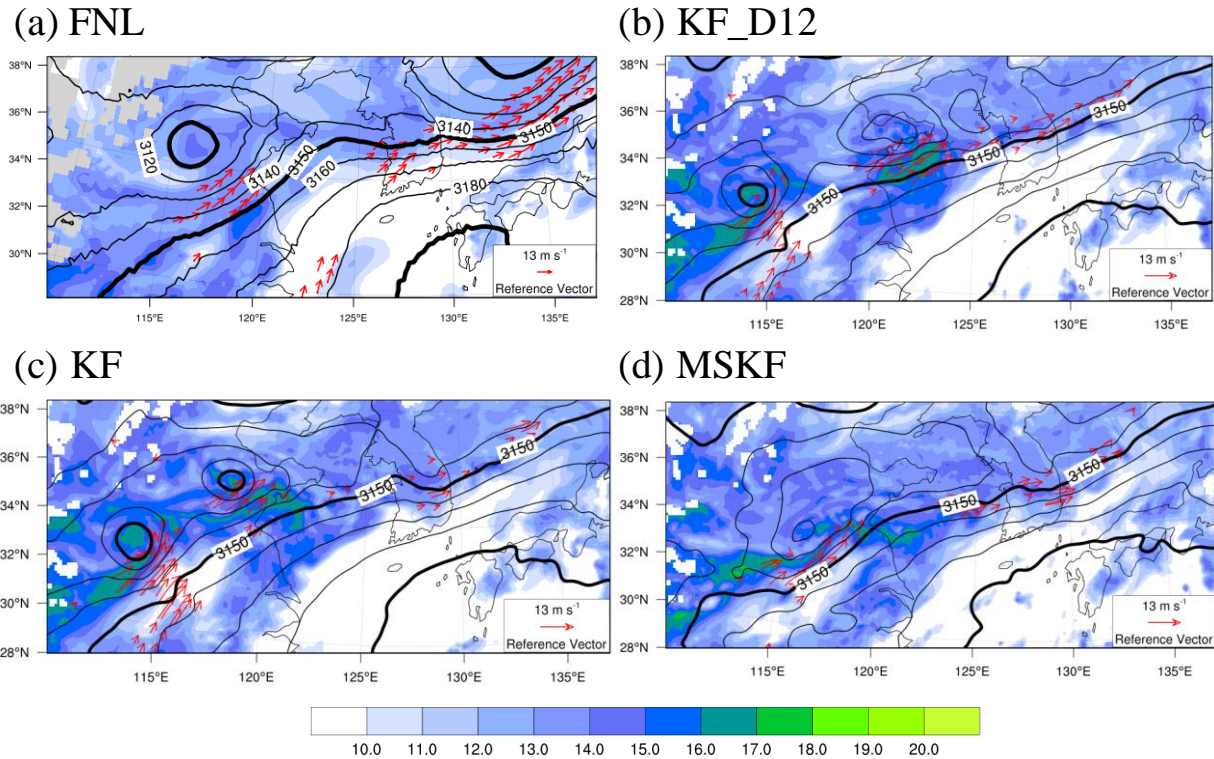
415

416

417

418

419



420

421 **Figure. 9.** Spatial contour maps of the wind ($>13 \text{ m s}^{-1}$, red vector), and water vapor (g kg^{-1} ,
 422 shaded) at 850 hPa, and geopotential height (m, black lines) at 700 hPa in the D02 domain at
 423 1800 UTC, 15 and 0000 UTC, 16 July 2017.

424

425 The locations of LLJ cores were consistent with those of the heavy precipitation area in
 426 the three runs, implying that LLJ played a significant role in the development of heavy
 427 precipitation by transporting wet and warm air from the subtropics. While the KF_D12 run only
 428 eliminated atmospheric instability by MPS in the D03 and D04 domains, the MPS could not
 429 adequately trigger convection over the Shandong Peninsula. The MPS unreasonably removed the
 430 atmospheric instability in the Yellow Sea rather than the peninsula. Additionally, the MPS
 431 prominently overestimated convection in the Yellow Sea, further increasing heavy precipitation
 432 in the region by enhancing LLJ and moisture convergence. Contrarily, subgrid-scale
 433 precipitation in the Shandong Peninsula in the KF run implied that convection was developed in

434 the proper location. However, the action of CPS was excessive, which led to the distortion of
435 synoptic fields such as intensified LLJs and increased moisture convergence in the Shandong
436 Peninsula and the Yellow Sea. Thereby, MPS also simulated considerable grid-scale
437 precipitation in the regions, indicating unreasonable overestimation of total precipitation by CPS
438 and MPS. However, in the MSKF run, subgrid-scale precipitation was decreased due to
439 decreasing role of CPS compared with that in the KF run. Therefore, similar to the IMERG, the
440 MSKF run reasonably captured torrential rainfall over the Shandong Peninsula associated with
441 CC2 and heavy precipitation in the Korean Peninsula related to CC1.

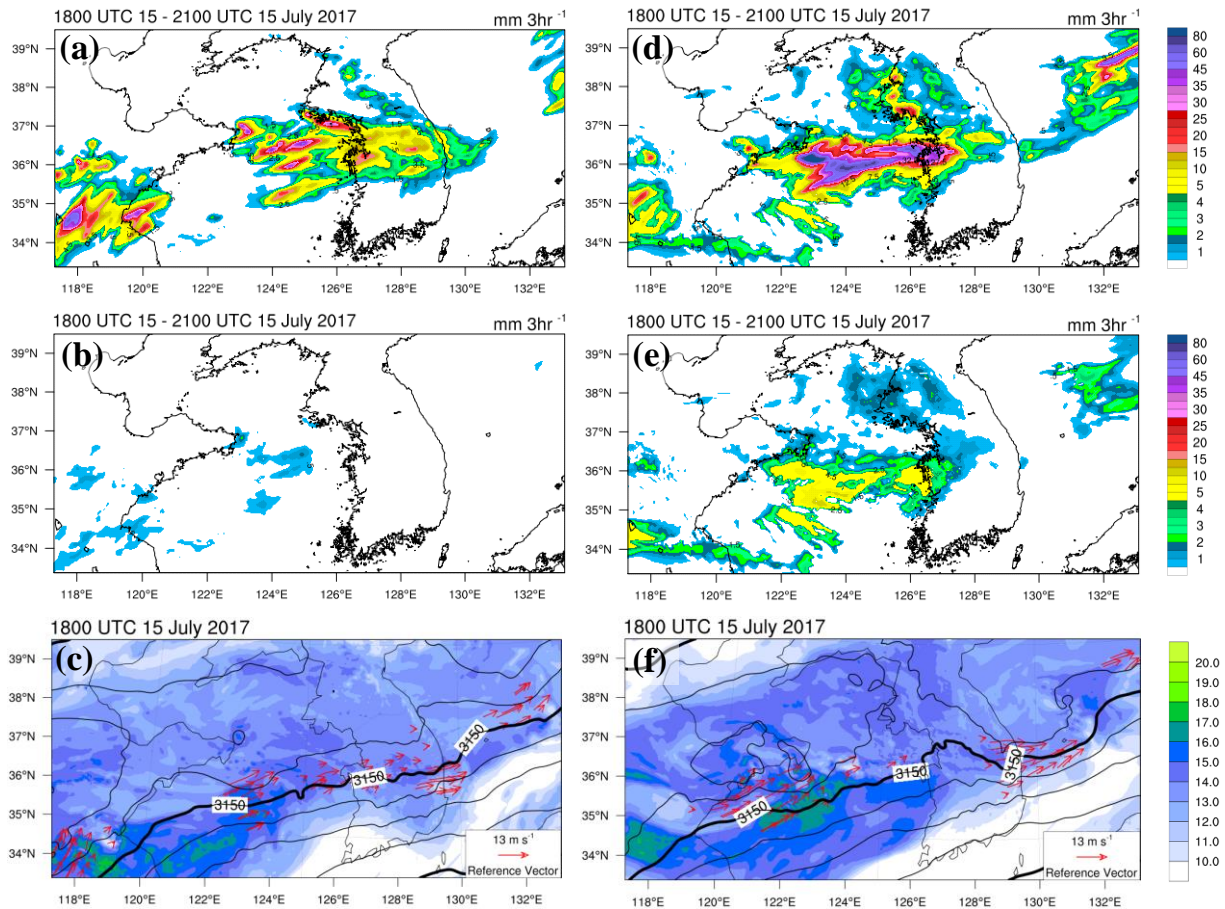
442 These results imply that high-resolution simulation of convective activities by MPS alone
443 could lead to inappropriate overestimation of precipitation, as atmospheric instability may not be
444 adequately reduced. Furthermore, CPS without scale-awareness may lead to the erroneous
445 simulation of heavy precipitation at high resolution due to the exaggeration of convection and
446 distortion of the synoptic fields. Therefore, the simulation of heavy precipitation using a high-
447 resolution model would require a scale-aware CPS.

448 3.2. Sensitivity run results for rainfall and synoptic environment

449 The previous section showed that the MSKF run improved the heavy precipitation
450 simulation in the Cheong-ju region compared to the KF_D12 and KF runs; because the MSKF
451 scheme represents an incorporative transition from the CPS-induced precipitation to MPS-
452 induced precipitation in the gray-zone. To investigate the reason for the improved simulation of
453 heavy precipitation in the MSKF run, we conducted two additional sensitivity experiments on the
454 scale-aware parameter of the MSKF scheme: (1) the CTS run, which modified the CAPE
455 timescale, and (2) the ENT run, which changed the entrainment rate.

456 Figure 10 shows the simulated total precipitation, subgrid-scale precipitation, and
457 synoptic fields reproduced by CTS and ENT runs. In Figure 10a, the CTS run captured the heavy
458 precipitation zones related to CC1 and CC2, similar to the MSKF run (see top panel of Figure
459 5d). However, the simulated precipitation zone in the Yellow Sea caused by CC1 was further
460 shifted westward, and subgrid-scale precipitation was simulated marginally more in the Yellow
461 Sea than in the MSKF run (Figure 10b), suggesting that the reduced CAPE timescale of the CTS
462 run compared to that of the MSKF run led to the faster removal of the atmospheric instability.
463 The reduced CAPE timescale of the CTS run resulted in the rapid development of convective
464 activities in the Yellow Sea rather than the Korean Peninsula (Figure 10b), which unreasonably
465 enhanced moisture convergence and LLJ at 850 hPa (Figure 10c). Thus, the CTS run simulated
466 grid-scale precipitation in the Yellow Sea earlier than in the MSKF run and corresponding
467 observation due to the distorted synoptic conditions. Contrastingly, the ENT run (Figure 10d)
468 unrealistically simulated the merged precipitation zone in the Yellow Sea, which is similar to the
469 KF run (Figure 5c). Compared to the CTS and MSKF runs, the ENT run tends to overestimate
470 subgrid-scale precipitation in the Yellow Sea because the entrainment rate was relatively weak
471 due to the absence of scale-aware parameters (Figure 10e). Therefore, the ENT run simulated
472 enhanced convective activities and excessive sub-grid precipitation in the Yellow Sea by CPS.
473 Furthermore, the enhanced convective activities led to the distortion of synoptic fields, such as
474 intensified LLJ and the exaggerated moisture convergence, which caused excessive grid-scale
475 precipitation in the Yellow Sea (Figure 10f). Therefore, the MSKF scheme could improve heavy
476 precipitation because of increasing CAPE timescale and enhanced entrainment process, which
477 led to modulating atmospheric instability. In other words, the subgrid-scale (grid-scale)
478 precipitation by the CPS (MPS) smoothly decreased (increase) in the MSKF run as the horizontal

479 resolution increased within the gray zone. The ENT run had a more significant error in simulated
 480 precipitation than in the CTS run, indicating that the enhanced entrainment rate of the MSKF
 481 scheme contributed more than the increased CAPE timescale to the improved simulation of
 482 heavy precipitation.



483

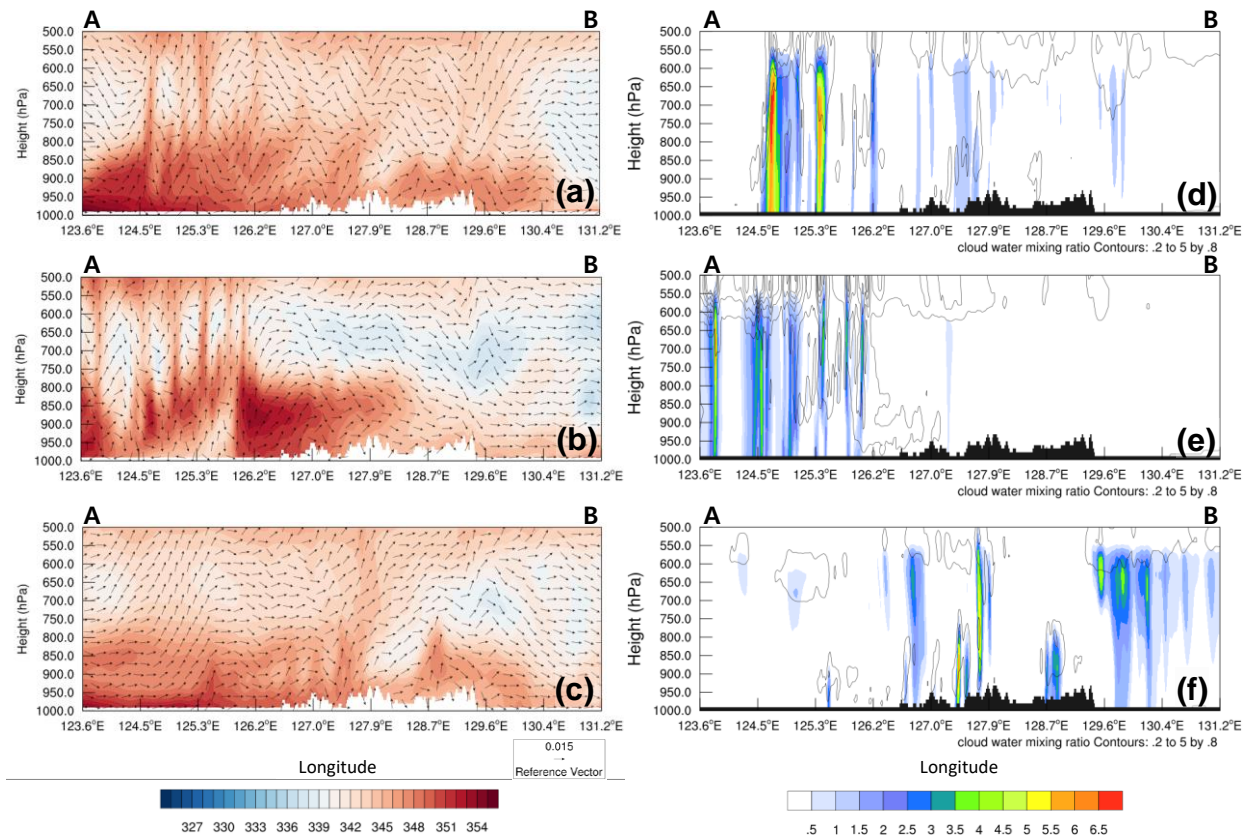
484 **Figure. 10.** Spatiotemporal maps of the (a, d) total precipitation (mm) and (b, e) convective
 485 precipitation (mm) between 1800 and 2100 UTC, 15 July 2017 (c, f) 850 hPa wind (m s⁻¹, red
 486 vector) and water vapor (g kg⁻¹, shaded), and 700 hPa geopotential height (m, black lines) at
 487 1800 UTC, 15 July 2017, in the D03 domains of the CTS (left panels) and the ENT runs (right
 488 panels).

489

490 To investigate the effect of scale-aware parameters on convective development, in Figure
491 11, we examined the vertical fields across the region where the difference in precipitation was
492 prominent between the sensitivity runs (see solid line in Figure 4b). The D04 domain results
493 were used to analyze the small-scale features, and the analysis time was 2100 UTC on 15 July ,
494 which was an appropriate time to examine the effects of the scale-aware parameter. Figure 11
495 shows a notable difference in the vertical distribution of the equivalent potential temperature
496 (EPT) as compared to those of the other experiments from the Yellow Sea (123.6 °E) to the
497 Cheong-ju region (127.9 °E). The CTS run simulated high EPT at the low-level in the Yellow
498 Sea, which increased atmospheric instability and then unreasonably developed intense
499 convective activities between 124.5 - 125.5 °E (Figure 11a). As shown in Figure 10b, the shorter
500 CAPE timescale in the CTS run than in the MSKF run triggered convection earlier in the Yellow
501 Sea rather than in the west coast of the Korean Peninsula. The earlier developed convection in
502 the Yellow Sea enhanced LLJ and moisture convergence, resulting in an increase in atmospheric
503 hydrometeors, which could cause excessive grid-scale precipitation (Figure 11d). Also,
504 convection was not prominently simulated in the inland of the Korean Peninsula, and relatively
505 fewer hydrometeors were resolved. Hence, torrential precipitation in Cheong-ju was not sensibly
506 captured (see Figure 10a). Similarly, the ENT run also simulated high EPT at the low-level. The
507 entrainment process, which mixed moist and warm air within convective clouds with dry and
508 cold environment air, was not strengthened because of the absence of a scale-aware parameter
509 (Figure 11b). High EPT led to an unstable atmosphere and overestimated convective
510 precipitation in the Yellow Sea, as shown in Figure 10b. The distorted LLJ and water vapor
511 convergence, resulting in increased atmospheric hydrometeors and then overestimated grid-scale
512 precipitation in most of the Yellow Sea regions. Since most hydrometeors were converted to

513 grid-scale precipitation in the Yellow Sea (Figure 11e), precipitation in the inland of the Korean
 514 Peninsula was considerably less, as shown in Figure 10d. On the other hand, the MSKF run
 515 realistically simulated low-level EPT, atmospheric stability, and hydrometeors in the Yellow Sea
 516 (Figure 11c and f). Therefore, it reproduced strong convection and more hydrometeors over the
 517 Cheong-ju region (127.9 °E), which resulted in a reasonable simulation of heavy precipitation by
 518 the CPS and MPS.

519



520

521 **Figure. 11.** Plots of the vertical cross-sections (AB in Figure 3b) of (a-c) equivalent potential
 522 temperature (K, shaded) and wind (m s⁻¹, vector), and (d-f) cloud hydrometeors mixing ratio (g
 523 kg⁻¹, shaded) and rain water mixing ratio (g kg⁻¹, contour) at 2100 UTC, 15 July 2017. Upper,
 524 middle, and lower panels indicate the CTS, ENT, and MSKF runs, respectively. Cloud
 525 hydrometeors are calculated by the summation of cloud water, ice, snow, and graupel.

526

527 **4 Conclusion**

528 This study investigated the impact of the scale-aware CPS across the gray-zone in the
529 WRF model on a heavy precipitation event over the Korean Peninsula. We selected the KF and
530 MSKF schemes as non-scale-aware CPS and scale-aware CPS, respectively. The MSKF scheme
531 uses a scale-aware parameter modifying the CAPE timescale and the entrainment process of the
532 KF scheme as a function of the horizontal grid spacing. The multi-nesting method is employed
533 with four domains with 36, 12, 4, and 1.33 km horizontal resolutions to consider the gray-zone
534 resolution.

535 According to our results, the KF runs (i.e., KF_D12 and KF runs) unreasonably
536 overestimated precipitation in the Yellow Sea and distorted synoptic fields such as LLJs and
537 moisture convergence. In the KF_D12 run, only the MPS resolved convective activities for the
538 domains with high-resolution (i.e., 4 and 1.33 km) and overestimated grid-scale precipitation in
539 the Yellow Sea because atmospheric instability is inadequately reduced. The CPS without scale-
540 awareness (i.e., KF run) also caused the erroneous precipitation simulation due to the
541 exaggeration of convection and distortion of the synoptic fields. Contrastingly, the MSKF run
542 realistically simulated precipitation and synoptic fields. And, the sensitivity experiments for the
543 scale-aware parameter (i.e., CTS and ENT runs) showed that the shorter CAPE timescale and
544 decreased entrainment process of the KF scheme compared with those of the MSKF scheme led
545 to the unreasonable fast development and exaggeration of convective activities, respectively.
546 Additionally, the ENT run has a more significant error in simulated precipitation than the CTS
547 run, suggesting that the enhanced entrainment process of the MSKF scheme contributes more to
548 the improved simulation of heavy precipitation than the increased CAPE timescale.
549 Consequently, the MSKF scheme with a scale-aware parameter realistically simulated

550 precipitation and synoptic fields by decreasing the subgrid-scale convection by the CPS and
551 increasing the grid-scale convection by MPS as the horizontal resolution increases.

552 As the horizontal resolution of numerical models for weather forecasting has increased
553 due to the remarkable advances in computing resources, more realistic grid-scale simulations are
554 required. Studies have shown that (*Jeworrek et al.*, 2019; *Hong&Dudhia*, 2012) scale-aware
555 physics schemes can improve the high-impact weather simulation when using very high-
556 resolution numerical models. This study also improved the understanding of the scale-aware CPS
557 role in heavy precipitation simulation at high-resolution. However, this study has some
558 limitations. Only the KF-based CPSs in the WRF model and a heavy rainfall case in the Korean
559 Peninsula are tested. Therefore, further experiments for the various scale-aware CPSs (e.g.,
560 scale-aware Grell-Freitas (*Grell&Freitas*, 2014) and gray-zone simplified Arakawa-Schubert
561 (*Kwon&Hong*, 2017)) should be conducted for more heavy precipitation. We could also plan
562 sensitivity tests using various combinations of the scale-aware CPSs and MPSs because the
563 predictability of convective systems associated with heavy rainfall can depend on these
564 combinations.

565 **Acknowledgments**

566 This work was partially funded by the 2020 Republic of Korea Airforce Numerical Weather
567 Prediction Research and Development Program, the development of Numerical Weather
568 Prediction and Data Application Techniques, and the Ulsan National Institute of Science and
569 Technology [Grant No. 1.210045.01].

570

571 **Data Availability Statement**

572 The National Centers for Environmental Prediction Global Final Analysis (NCEP-FNL) data
573 are available online (<https://rda.ucar.edu/datasets/ds083.2/> and
574 <https://rda.ucar.edu/datasets/ds083.3/>). IMERG was provided by the NASA Goddard Space
575 Flight Center's IMERG and PPS teams, which develop and compute IMERG as a contribution
576 to the GPM mission, and archived at the NASA GES DISC
577 (https://disc.gsfc.nasa.gov/datasets/GPM_3IMERGHH_V06/summary) and online
578 (<https://gpm.nasa.gov/data/directory>).

579

580 **Reference**

581 Alapaty, K., Herwehe, J. A., Otte, T. L., Nolte, C. G., Bullock, O. R., Mallard, M. S., Kain, J. S., and Dudhia, J.
582 (2012), Introducing subgrid-scale cloud feedbacks to radiation for regional meteorological and climate modeling,
583 *39*(24), doi:<https://doi.org/10.1029/2012GL054031>.
584 Arakawa, A., Jung, J.-H., and Wu, C.-M. J. M. m. (2016), Multiscale modeling of the moist-convective atmosphere,
585 *56*, 16.11-16.17.
586 Arakawa, A., Jung, J. H., and Wu, C. M. (2011), Toward unification of the multiscale modeling of the atmosphere,
587 *Atmos. Chem. Phys.*, *11*(8), 3731-3742, doi:10.5194/acp-11-3731-2011.
588 Bechtold, P., Bazile, E., Guichard, F., Mascart, P., and Richard, E. J. Q. J. o. t. R. M. S. (2001), A mass-flux
589 convection scheme for regional and global models, *127*(573), 869-886.
590 Bechtold, P., Koehler, M., Jung, T., Doblas-Reyes, F., Leutbecher, M., Rodwell, M. J., Vitart, F., Balsamo, G. J. Q.
591 J. o. t. R. M. S. A. j. o. t. a. s., applied meteorology, and oceanography, p. (2008), *Advances in simulating*
592 *atmospheric variability with the ECMWF model: From synoptic to decadal time-scales*, *134*(634), 1337-1351.
593 Bechtold, P., Semane, N., Lopez, P., Chaboureaud, J.-P., Beljaars, A., and Bormann, N. J. J. o. A. S. (2014),
594 Representing equilibrium and nonequilibrium convection in large-scale models, *71*(2), 734-753.
595 Bengtsson, L., and Körnich, H. (2016), Impact of a stochastic parametrization of cumulus convection, using cellular
596 automata, in a mesoscale ensemble prediction system, *142*, 1150-1159.

- 597 Charles, M. E., Colle, B. A. J. W., and forecasting (2009), Verification of extratropical cyclones within the NCEP
598 operational models. Part I: Analysis errors and short-term NAM and GFS forecasts, *24*(5), 1173-1190.
- 599 Cho, N.-S., and Lee, T.-Y. J. A.-P. J. o. A. S. (2006), A numerical study of multiple convection bands over the
600 Korean peninsula, *42*(2), 87-105.
- 601 Choi, G., Kwon, W.-T., Boo, K.-O., and Cha, Y.-M. J. et al. (2008), Recent spatial and temporal changes in means
602 and extreme events of temperature and precipitation across the Republic of Korea, *43*(5), 681-700.
- 603 Choi, Y., Lee, H., and Kwon, J. J. T. g. j. o. K. (2013), Recent change on frequency-magnitude of summer extreme
604 rainfall events over the Republic of Korea, *47*(1), 83-97.
- 605 Chung, Y., Kim, H. J. A. Q., Atmosphere, and Health (2019), Observations on changes in Korean Changma rain
606 associated with climate warming in 2017 and 2018, *12*(2), 197-215.
- 607 Davies, T., Cullen, M. J., Malcolm, A. J., Mawson, M., Staniforth, A., White, A., Wood, N. J. Q. J. o. t. R. M. S. A.
608 j. o. t. a. s., applied meteorology, and oceanography, p. (2005), A new dynamical core for the Met Office's global
609 and regional modelling of the atmosphere, *131*(608), 1759-1782.
- 610 Deng, A., Stauffer, D. R. J. J. o. a. m., and climatology (2006), On improving 4-km mesoscale model simulations,
611 *45*(3), 361-381.
- 612 Dudhia, J. J. J. o. t. a. s. (1989), Numerical study of convection observed during the winter monsoon experiment
613 using a mesoscale two-dimensional model, *46*(20), 3077-3107.
- 614 Dudhia, J. J. O. T. (2005), Chapter 8: Part II: Physics Options in MM5.
- 615 Emanuel, K. A., and Raymond, D. J. (1993), THE REPRESENTATION OF CUMULUS CONVECTION IN
616 NUMERICAL MODELS %J Meteorological Monographs, *24*(46), 1-246, doi:10.1175/0065-9401-24.46.1.
- 617 Freitas, S. R., Grell, G. A., Molod, A., Thompson, M. A., Putman, W. M., Santos e Silva, C. M., and Souza, E. P.
618 (2018), Assessing the Grell-Freitas Convection Parameterization in the NASA GEOS Modeling System, *10*(6),
619 1266-1289, doi:<https://doi.org/10.1029/2017MS001251>.
- 620 Fritsch, J. M., and Chappell, C. F. (1980), Numerical Prediction of Convectively Driven Mesoscale Pressure
621 Systems. Part I: Convective Parameterization %J Journal of Atmospheric Sciences, *37*(8), 1722-1733,
622 doi:10.1175/1520-0469(1980)037<1722:Npocdm>2.0.Co;2.
- 623 Fritsch, M. J., Chappell, C. F., and Hoxit, L. R. (1976), The Use of Large-Scale Budgets for Convective
624 Parameterization %J Monthly Weather Review, *104*(11), 1408-1418, doi:10.1175/1520-
625 0493(1976)104<1408:Tuolsb>2.0.Co;2.
- 626 Gerard, L. J. Q. J. o. t. R. M. S. A. j. o. t. a. s., applied meteorology, and oceanography, p. (2007), An integrated
627 package for subgrid convection, clouds and precipitation compatible with meso-gamma scales, *133*(624), 711-730.
- 628 Grell, G. A., and Freitas, S. R. J. A. C. (2014), A scale and aerosol aware stochastic convective parameterization for
629 weather and air quality modeling, %J *Atmospheric Chemistry*
630 *Physics*, *14*(10), 5233-5250.
- 631 Gustafson, J. W. I., Ma, P. L., Xiao, H., Singh, B., Rasch, P. J., and Fast, J. D. J. J. o. G. R. A. (2013), The Separate
632 Physics and Dynamics Experiment (SPADE) framework for determining resolution awareness: A case study of
633 microphysics, *118*(16), 9258-9276.
- 634 Ha, K.-J., Park, S.-K., and Kim, K.-Y. (2005), On interannual characteristics of Climate Prediction Center merged
635 analysis precipitation over the Korean peninsula during the summer monsoon season, *25*(1), 99-116,
636 doi:<https://doi.org/10.1002/joc.1116>.
- 637 Han, J., Pan, H.-L. J. W., and Forecasting (2011), Revision of convection and vertical diffusion schemes in the
638 NCEP Global Forecast System, *26*(4), 520-533.
- 639 Ho, C.-H., and Kang, I.-S. J. J. K. M. S. (1988), The variability of precipitation in Korea, *24*(1), 38-48.
- 640 Ho, C. H., Lee, J. Y., Ahn, M. H., and Lee, H. S. (2003), A sudden change in summer rainfall characteristics in
641 Korea during the late 1970s, *Int J Climatol*, *23*(1), 117-128, doi:10.1002/joc.864.
- 642 Hong, S.-Y., and Dudhia, J. (2012), Next-Generation Numerical Weather Prediction: Bridging Parameterization,
643 Explicit Clouds, and Large Eddies %J Bulletin of the American Meteorological Society, *93*(1), ES6-ES9,
644 doi:10.1175/2011bams3224.1.
- 645 Hong, S.-Y., and Lee, J.-W. J. A. R. (2009), Assessment of the WRF model in reproducing a flash-flood heavy
646 rainfall event over Korea, *93*(4), 818-831.
- 647 Hong, S.-Y., and Lim, J.-O. J. J. A.-P. J. o. A. S. (2006), The WRF single-moment 6-class microphysics scheme
648 (WSM6), *42*(2), 129-151.
- 649 Hong, S.-Y., Noh, Y., and Dudhia, J. (2006), A New Vertical Diffusion Package with an Explicit Treatment of
650 Entrainment Processes %J Monthly Weather Review, *134*(9), 2318-2341, doi:10.1175/mwr3199.1.
- 651 Huffman, G. J., Bolvin, D. T., Braithwaite, D., Hsu, K., Joyce, R., Xie, P., and Yoo, S.-H. J. A. T. B. D. V. (2015a),
652 NASA global precipitation measurement (GPM) integrated multi-satellite retrievals for GPM (IMERG), *4*, 26.

- 653 Huffman, G. J., Bolvin, D. T., Nelkin, E. J., and Tan, J. J. N. G. C. (2015b), Integrated Multi-satellite Retrievals for
654 GPM (IMERG) technical documentation, *612*(47), 2019.
- 655 Jankov, I., Schultz, P. J., Anderson, C. J., and Koch, S. E. J. J. o. H. (2007), The impact of different physical
656 parameterizations and their interactions on cold season QPF in the American River basin, *8*(5), 1141-1151.
- 657 Jeworrek, J., West, G., and Stull, R. (2019), Evaluation of Cumulus and Microphysics Parameterizations in WRF
658 across the Convective Gray Zone %J Weather and Forecasting, *34*(4), 1097-1115, doi:10.1175/waf-d-18-0178.1.
- 659 Kain, J. S. J. J. o. a. m. (2004), The Kain–Fritsch convective parameterization: an update, *43*(1), 170-181.
- 660 Kang, I.-S., Ho, C.-H., and Min, K.-D. J. J. o. K. M. S. (1992), Long-range forecast of summer precipitation in
661 Korea, *28*(3), 283-292.
- 662 Khairoutdinov, M., and Randall, D. J. J. o. A. S. (2006), High-resolution simulation of shallow-to-deep convection
663 transition over land, *63*(12), 3421-3436.
- 664 Kim, C., Seo, M.-S., and Atmosphere, k. J. (2008), Change-Point in the Recent (1976-2005) Precipitation over
665 South Korea, *18*(2), 113-122.
- 666 Kuang, Z., and Bretherton, C. S. J. J. o. t. A. S. (2006), A mass-flux scheme view of a high-resolution simulation of
667 a transition from shallow to deep cumulus convection, *63*(7), 1895-1909.
- 668 Kwon, M., Jhun, J.-G., and Ha, K.-J. (2007), Decadal change in east Asian summer monsoon circulation in the mid-
669 1990s, *34*(21), doi:<https://doi.org/10.1029/2007GL031977>.
- 670 Kwon, Y. C., and Hong, S.-Y. (2017), A Mass-Flux Cumulus Parameterization Scheme across Gray-Zone
671 Resolutions %J Monthly Weather Review, *145*(2), 583-598, doi:10.1175/mwr-d-16-0034.1.
- 672 Lee, S.-H., Kim, E.-K., and Heo, I.-H. J. J. o. t. K. a. o. r. g. (2011a), A study on variability of extreme precipitation
673 by basin in South Korea, *17*(5), 505-520.
- 674 Lee, S.-W., Lee, D.-K., and Chang, D.-E. J. A. i. A. S. (2011b), Impact of horizontal resolution and cumulus
675 parameterization scheme on the simulation of heavy rainfall events over the Korean Peninsula, *28*(1), 1-15.
- 676 Lee, T.-Y., and Kim, Y.-H. (2007), Heavy Precipitation Systems over the Korean Peninsula and their Classification,
677 *Asia-Pacific Journal of the Atmospheric Sciences*, *43*, 367-396.
- 678 Lin, C., and Arakawa, A. J. J. o. t. a. s. (1997), The macroscopic entrainment processes of simulated cumulus
679 ensemble. Part I: Entrainment sources, *54*(8), 1027-1043.
- 680 Lin, Y., Zhao, M., Ming, Y., Golaz, J.-C., Donner, L. J., Klein, S. A., Ramaswamy, V., and Xie, S. (2013),
681 Precipitation Partitioning, Tropical Clouds, and Intraseasonal Variability in GFDL AM2 %J Journal of Climate,
682 *26*(15), 5453-5466, doi:10.1175/jcli-d-12-00442.1.
- 683 Lowrey, M. R. K., and Yang, Z.-L. (2008), Assessing the capability of a regional-scale weather model to simulate
684 extreme precipitation patterns and flooding in central Texas, %J Weather
685 *Forecasting*, *23*(6), 1102-1126.
- 686 Mishra, S. K., and Srinivasan, J. (2010), Sensitivity of the simulated precipitation to changes in convective
687 relaxation time scale, paper presented at Annales Geophysicae, Copernicus GmbH.
- 688 Mlawer, E. J., Taubman, S. J., Brown, P. D., Iacono, M. J., and Clough, S. A. (1997), Radiative transfer for
689 inhomogeneous atmospheres: RRTM, a validated correlated-k model for the longwave, *102*(D14), 16663-16682,
690 doi:<https://doi.org/10.1029/97JD00237>.
- 691 MOIS (2019), Ministry of Interior and Safety (MOIS). <https://www.mois.go.kr/frt/a01/frtMain.do>.
- 692 Molinari, J., and Dudek, M. J. M. W. R. (1992), Parameterization of convective precipitation in mesoscale
693 numerical models: A critical review, *120*(2), 326-344.
- 694 Mun, T., Park, C., Kim, G., and Cha, D.-H. (2019), Long-term Variability of Summer Heavy Rainfall in the Seoul
695 Metropolitan Area, *14*(4), 209-219.
- 696 Noh, Y., Cheon, W. G., Hong, S. Y., and Raasch, S. (2003), Improvement of the K-profile Model for the Planetary
697 Boundary Layer based on Large Eddy Simulation Data, *Boundary-Layer Meteorology*, *107*(2), 401-427,
698 doi:10.1023/A:1022146015946.
- 699 Olson, D. A., Junker, N. W., and Korty, B. (1995), Evaluation of 33 Years of Quantitative Precipitation Forecasting
700 at the NMC %J Weather and Forecasting, *10*(3), 498-511, doi:10.1175/1520-
701 0434(1995)010<0498:Eoyopp>2.0.Co;2.
- 702 Park, C.-Y., Moon, J.-Y., Cha, E.-J., Yun, W.-T., and Choi, Y.-E. J. J. o. t. K. G. S. (2008), Recent changes in
703 summer precipitation characteristics over South Korea, *43*(3), 324-336.
- 704 Prein, A. F., Langhans, W., Fossier, G., Ferrone, A., Ban, N., Goergen, K., Keller, M., Tölle, M., Gutjahr, O., and
705 Feser, F. J. R. o. g. (2015), A review on regional convection-permitting climate modeling: Demonstrations,
706 prospects, and challenges, *53*(2), 323-361.
- 707 Saito, K., Fujita, T., Yamada, Y., Ishida, J.-i., Kumagai, Y., Aranami, K., Ohmori, S., Nagasawa, R., Kumagai, S.,
708 and Muroi, C. J. M. W. R. (2006), The operational JMA nonhydrostatic mesoscale model, *134*(4), 1266-1298.

- 709 Shin, C.-S., and Lee, T.-Y. *J. J. o. t. M. S. o. J. S. I.* (2005), Development mechanisms for the heavy rainfalls of 6-7
710 August 2002 over the middle of the Korean Peninsula, *83*(5), 683-709.
- 711 Sims, A. P., Alapaty, K., and Raman, S. J. M. w. r. (2017), Sensitivities of summertime mesoscale circulations in the
712 coastal Carolinas to modifications of the Kain–Fritsch cumulus parameterization, *145*(11), 4381-4399.
- 713 Sun, J., and Lee, T.-Y. *J. J. o. t. M. S. o. J. S. I.* (2002), A numerical study of an intense quasi-stationary convection
714 band over the Korean Peninsula, *80*(5), 1221-1245.
- 715 Tokioka, T., Yamazaki, K., Kitoh, A., and Ose, T. *J. J. o. t. M. S. o. J. S. I.* (1988), The equatorial 30-60 day
716 oscillation and the Arakawa-Schubert penetrative cumulus parameterization, *66*(6), 883-901.
- 717 Wang, H., Zhang, M., and Liu, M. *J. o. A. M. S.* (2006), Influence of Moist Schemes in MM5 on the Uncertainties
718 of “03·7” Heavy Rainfall Numerical simulation, *17*(3), 346-353.
- 719 Wang, S., Sobel, A. H., Zhang, F., Sun, Y. Q., Yue, Y., and Zhou, L. *J. o. C.* (2015), Regional simulation of the
720 October and November MJO events observed during the CINDY/DYNAMO field campaign at gray zone resolution,
721 *28*(6), 2097-2119.
- 722 Wang, W., and Seaman, N. L. (1997), A Comparison Study of Convective Parameterization Schemes in a Mesoscale
723 Model *J Monthly Weather Review*, *125*(2), 252-278, doi:10.1175/1520-0493(1997)125<0252:Acsocp>2.0.Co;2.
- 724 Weisman, M. L., Skamarock, W. C., and Klemp, J. B. *J. M. W. R.* (1997), The resolution dependence of explicitly
725 modeled convective systems, *125*(4), 527-548.
- 726 Yang, M.-J., Chien, F.-C., Cheng, M.-D. *J. T., Atmospheric, and Sciences, O.* (2000), Precipitation Parameterization
727 in a Simulated Mei-Yu Front, *11*(2), 393-422.
- 728 Yu, X., Lee, T.-Y. *J. T. A. D. M., and Oceanography* (2010), Role of convective parameterization in simulations of
729 a convection band at grey-zone resolutions, *62*(5), 617-632.
- 730 Zheng, Y., Alapaty, K., Herwehe, J. A., Del Genio, A. D., and Niyogi, D. *J. M. W. R.* (2016), Improving high-
731 resolution weather forecasts using the Weather Research and Forecasting (WRF) Model with an updated Kain–
732 Fritsch scheme, *144*(3), 833-860.